Influence of lattice-preferred orientation with respect to magnetizing field on intensity of remanent magnetization in polycrystalline hemo-ilmenite

Article *in* Geophysical Journal International · February 2013

DOI: 10.1093/gji/ggs046

CITATIONS
12

READS
49

4 authors, including:

Karl Fabian
Norges geologiske undersøkelse
181 PUBLICATIONS **2,204** CITATIONS
SEE PROFILE

Suzanne McEnroe
Norwegian University of Science and Technology
149 PUBLICATIONS **1,672** CITATIONS
SEE PROFILE

F. Heidelbach
University of Bayreuth
120 PUBLICATIONS **2,203** CITATIONS
SEE PROFILE

Geophysical Journal International Advance Access published November 30, 2012

Geophys. J. Int. (2012) doi: 10.1093/gji/ggs046

Influence of lattice-preferred orientation with respect to magnetizing field on intensity of remanent magnetization in polycrystalline hemo-ilmenite

P. Robinson,[1] K. Fabian,[1] S. A. McEnroe[2] and F. Heidelbach[3]

[1] *Geological Survey of Norway,* 7491 *Trondheim, Norway. E-mail: peter.robinson@ngu.no*
[2] *Norwegian University of Science and Technology,* 7491 *Trondheim, Norway*
[3] *Bayerisches Geoinstitut,* 95440 *Bayreuth, Germany*

Accepted 2012 October 24. Received 2012 October 24; in original form 2012 May 25

SUMMARY

New experimental and computational approaches to interpret orientation and intensity of natural remanent magnetization (NRM) carried by lamellar magnetism are applied to historic magnetic measurements on a collection of 82 massive hemo-ilmenite samples from the Allard Lake District in the Grenville Province, Quebec. The anisotropy of magnetic susceptibility (AMS), together with declination and inclination of NRM, indicate a systematic deflection β of the NRM vector away from the unit vector **v** that represents the Mesoproterozoic magnetizing field direction. The deflection β is caused by a statistical lattice-preferred orientation (LPO) of the individual (0001) basal planes, to which the NRM is confined in hemo-ilmenite crystals. Here, we study a second deflection ψ that is the angle the NRM makes with the statistical (0001) basal plane of the crystal assemblage, in relation to the angle α between the statistical (0001) basal plane and **v**. The relation between these two angles depends on the scatter of the distribution of crystal platelets, which also influences the AMS of the assemblage. For a Fisher distribution of basal planes, the distribution parameter K can be determined from ψ and α. It is then further possible to infer the single-crystal anisotropy of individual platelets. Typical crystals of hemo-ilmenite turn out to have a relatively weak AMS so that samples with a narrow Fisher distribution of platelets nevertheless can have a weak AMS. This has been confirmed in two samples by measurement of the (0001) basal plane distribution of crystals using electron backscatter diffraction, and in one of these two samples by measuring AMS and NRM of a single hemo-ilmenite crystal. Based on our estimated K values for selected samples, we calculate values of β, NRM intensity and ψ for any value of α. These data provide striking examples of the influence of the orientation of the crystal LPO on the intensity of lamellar magnetism, and explain the large variation of observed NRM intensities by varying orientation with respect to the magnetizing field, without requiring large variations of the paleomagnetic field intensity. This relation between NRM and LPO is also important for anomaly interpretation in areas with strong foliation.

Key words: Magnetic anomalies: modeling and interpretation; Magnetic fabrics and anisotropy; Magnetic mineralogy and petrology; Palaeointensity; Palaeomagnetism applied to tectonics; Microstructures.

1 INTRODUCTION

1.1 Background

The hemo-ilmenite deposits associated with massif anorthosites of the Allard Lake region of the Mesoproterozic Grenville Province, Quebec, Canada, include the Lac Tio Deposit, containing the world's largest ilmenite mine. The deposits were located by aeromagnetic surveys in the early 1940's and related ground-magnetic studies (Hammond 1952; Bourret 1959). Aeromagnetic maps show magnetic lows (below background) associated with the deposits and parts of the anorthosites; however, high-amplitude negative magnetic anomalies are more common over the hemo-ilmenite deposits. The early studies confirmed that these anomalies were caused by strong natural remanent magnetization (NRM) in a direction at an obtuse angle ($\approx$160°) to the present Earth's magnetic field. The ratio of induced magnetization (J_i) to remanent magnetization (J_r) shows the extremely high contribution from the NRM to the anomalies. The average Q value (J_r/J_i) for the entire Hargraves data set is 155, with values ranging from 7 to 990, clearly indicating that the NRM

vector dominates the anomaly response. This historic data set of AMS and NRM data of Hargraves (1959a,b) from the Allard Lake region gave us the opportunity to elucidate features which have an important influence on the intensity of magnetization from samples with similar bulk compositions and cooling history but variations in orientation of the mineral foliation with respect to the magnetizing field.

In hemo-ilmenite crystals, the NRM is virtually confined to the rhombohedral (0001) basal plane. Within the studied massive ore samples, there is a strong lattice-preferred orientation (LPO) of basal planes rarely oriented parallel to the ancient magnetic field. Accordingly, the hemo-ilmenite ores cannot be used in the conventional way to determine paleomagnetic vectors (Hargraves 1959a). Hargraves (1959a,b) determined the ancient field direction by measuring the NRM and the anisotropy of magnetic susceptibility (AMS) of a large number of samples. These samples and results, in addition to new measurements, provide the basis for the present study. Hargraves (1959a) included data on 51 samples from the Lac Tio Deposit, and Hargraves (1959b) contains similar data on six samples from the Lac Ellen Deposit, six from the Grader Deposit, six from the Northwest Arm Deposit, and 13 from the Lac Allard deposits, giving a total of 82 samples.

The magnetic features of the Lac Tio and related deposits near Allard Lake, Quebec, are summarized in (McEnroe *et al.* 2007b). Key aspects include two magnetic properties of hemo-ilmenite crystals: 1) the magnetization is located in or close to the (0001) basal plane and 2) there is an AMS, with highest susceptibility parallel to the basal plane and weakest parallel to the crystallographic *c*-axis. Hargraves (1959a) used AMS measurements to show that the hemo-ilmenite ores have a moderate to strong LPO, with statistical basal planes oriented apparently parallel to the irregular basal contact of the ore body, and geographically at various angles to the estimated Mesoproterozoic magnetizing field. This prevented the NRM of most samples from being oriented parallel to the field, but lie as close to the field vector as the dominant crystal directions would allow. Based on AMS and NRM orientations, Hargraves (1959a) graphically determined the paleofield direction. His paleomagnetic results agree well with those determined later by several techniques for a larger collection of rocks in the district (Hargraves & Burt 1967).

The results presented here have implications for several areas of geophysical research. Strong and stable remanent magnetization is well known in rocks where exsolved rhombohedral oxides are the main magnetic carrier. In these cases, the effects of LPO must be understood and overcome in the determination of paleomagnetic vectors. Here, we find the earlier approaches of Hargraves (1959a,b) fully vindicated. Successful interpretation of magnetic anomalies over rocks containing exsolved members of the hematite-ilmenite solid solution series relies on a fundamental understanding of their remanent magnetization. This is essential, for example, in exploration for hemo-ilmenite ore deposits. In this paper, the relationship between the intensity of remanent magnetization and the angle of the LPO to the magnetizing field during remanence acquisition is quantitatively studied. Different parts of the same body of rock, with the same mineralogy and cooling history, can show vastly different remanence intensities, merely due to different directions of the LPO. As a consequence, the local variation of NRM vectors produced by LPO must be recorded, and incorporated into the interpretation of magnetic anomalies. Further, that effect will have essentially no relationship with the present magnetic field, but only with the paleofield when magnetization was acquired. Beyond these more practical matters, unraveling the different influences of crystallography upon direction and intensity of remanent magnetization, and magnetic susceptibility is a worthy subject of exploration for its own sake on the road to new understanding, which may have unforeseen applications in other fields, for example, planetary magnetism.

1.2 Lamellar magnetism and Lac Tio hemo-ilmenite

The magnetic properties of igneous and metamorphic rocks containing ilmenite with hematite exsolution lamellae (hemo-ilmenite) and hematite with ilmenite exsolution lamellae (ilmeno-hematite) (McEnroe & Brown 2000; McEnroe *et al.* 2001, 2002, 2007a) have been found to result from an interface phenomenon called *lamellar magnetism* (Harrison & Becker 2001; Robinson *et al.* 2002, 2004, 2006a,b). The samples are characterized by strong and very stable remanent magnetization, resulting from uncompensated spins provided by magnetically interacting contact layers on two sides of nanometre-scale exsolution lamellae. The NRM is likely produced at the moment of creation of interfaces during exsolution within the thermo-chemical region where CAF hematite is stable (Robinson *et al.* 2002, 2004; Fabian *et al.* 2008). Hence, it is rather a chemical than a thermal remanent magnetization. The NRM intensity is proportional to the total area of exsolution interfaces, thus enhanced by very fine-scale exsolution (McCammon *et al.* 2009). Short-term thermal demagnetization experiments show that the magnetization is lost at approximately the Neél temperature of hematite lamellae. The NRM is highest in a crystal, when the moments of all lamellae are aligned (in-phase) in one direction along a single one of three possible sub-lattice directions in the basal (0001) plane, and can approach zero, when the moments are equally distributed (out-of-phase) in either direction along any of the three sub-lattice directions.

Collaboration with Hargraves on the Lac Tio hemo-ilmenite led to the hypothesis that in addition to external-field intensity, the intensity of the lamellar NRM is also controlled by the orientation of the (0001) basal planes of the rhombohedral-oxide crystals with respect to the magnetizing field during exsolution (Robinson *et al.* 2002, 2004). In-phase lamellae are energetically favourable when the field is parallel to (0001) so that the lamellar moment is aligned with the external field. In contrast, when the magnetic field is oriented normal to (0001), it cannot favour in-phase lamellae. In fig. 9 of Hargraves (1959a), corresponding to the black symbols in Fig. 1, there is a negative correlation between NRM intensity and the angle between the statistical (0001) basal plane and the magnetizing field direction. The orientations of the basal plane were determined statistically using AMS, where the minimal susceptibility k_3 in these rhombohedral oxides is parallel to the *c*-crystallographic axis, and the largest susceptibility eigenvalues k_1 and k_2 are measured parallel to (0001) (see Hrouda *et al.* 1985). These relationships were confirmed later for exsolved crystals of hemo-ilmenite, using a combination of electron backscatter diffraction (EBSD) and AMS (Robinson *et al.* 2006b).

2 GEOMETRIC RELATIONS IN HEMO-ILMENITE CRYSTALS AND ASSEMBLAGES

Here, the data of Hargraves (1959a,b) are presented, together with new measurements, to focus systematically on the relationship between NRM and AMS, which is essential for comparison with our theoretical considerations developed below.

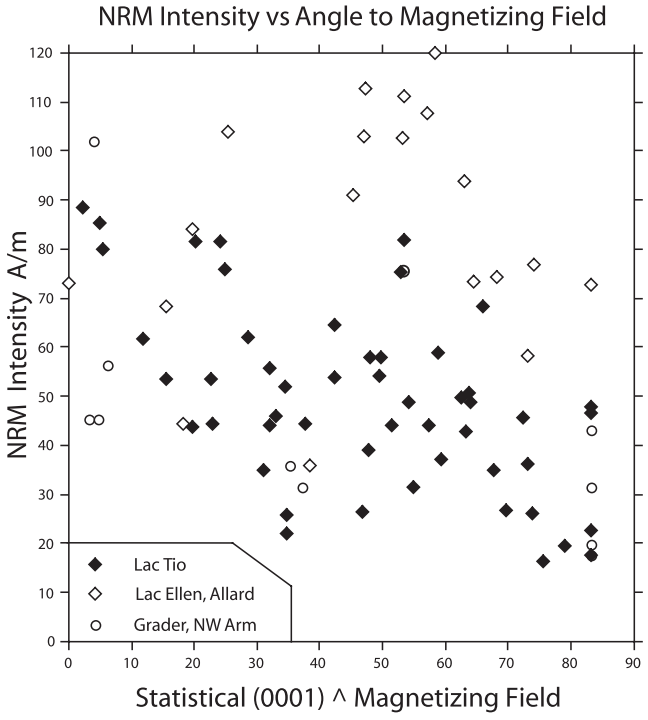

Figure 1. NRM intensity versus angle between statistical (0001) and magnetizing field. This plot includes all data and is a follow-on to the original figure of Hargraves (1959a).

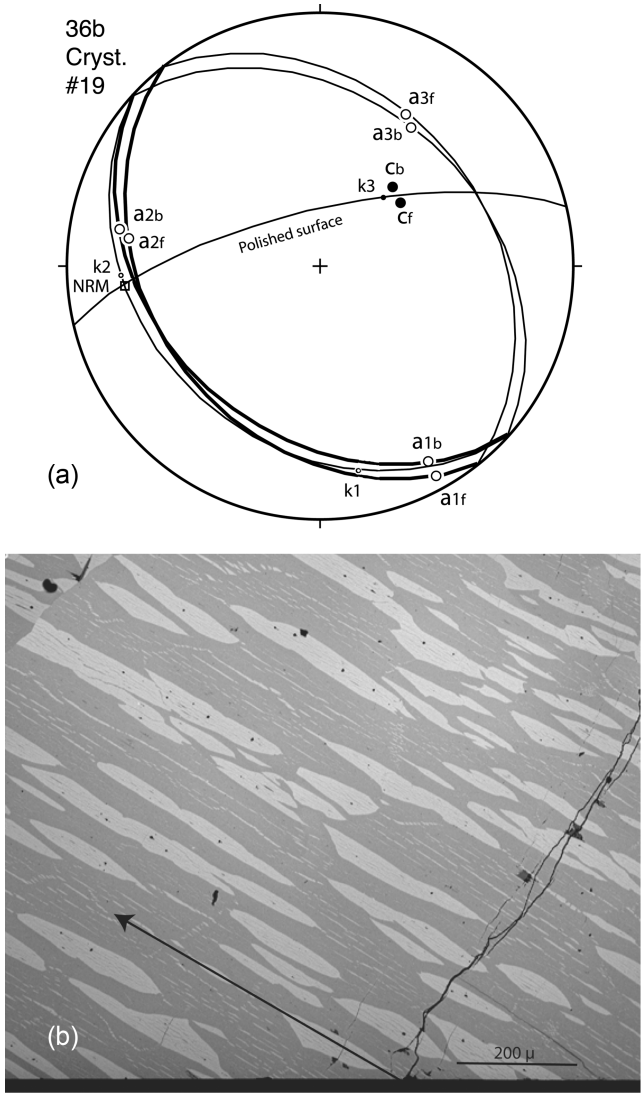

Figure 2. (a) Equal area diagram for crystal #19, sample AL36b, showing crystallographic axes determined by EBSD, k_1-, k_2- and k_3-axes of AMS and NRM. The (0001) basal plane containing the *a*-crystallographic axes is shown in both lower hemisphere (BOLD LINE) and upper hemisphere (thinner line). The GC containing the k_1- and k_2-axes of the AMS is shown only in the lower hemisphere. All points are in the lower hemisphere except a3. (b) Electron backscatter image of same crystal cut normal to the (0001) basal plane and also parallel to the NRM vector.

2.1 Magnetic relationships in single crystals

Single crystals from sample 36b were isolated by first identifying locations on polished front and back surfaces of a 0.6-cm-thick slab using EBSD, see Robinson *et al.* (2006b) also Fabian *et al.* (2011). Those locations were selected which showed the same, or nearly the same, crystallographic *c*- and *a*-axis positions on both sides. Six cores of diameter 5 mm were drilled from selected sites. Of these only one showed excellent coincidence of the front and back crystallographic axes. For this core (crystal #19), the relationships are illustrated in an equal area diagram in Fig. 2(a). The points labelled cf and cb are the *c*-axis locations on front and back surfaces, respectively, whereas a1f, a1b, a2f, a2b, a3f and a3b are the *a*-axis locations on front and back. The AMS was measured, including intensities and the orientations of the three axes of the AMS ellipsoid. The k_3-axis of minimum susceptibility coincides closely with the *c*-axis determined by EBSD, whereas the plane of the k_1- and k_2-axes corresponds closely to the (0001) basal plane containing the *a*-axes. The plot shows that the NRM of crystal #19 lies exactly in the $k_1 - k_2$ plane determined by its AMS, very close to the k_2-axis of the AMS, and only a few degrees from the a_2-axes determined by EBSD. A polished surface was cut through the crystal at an angle normal to the (0001) basal plane and also parallel to the NRM direction in that plane. Fig. 2(b) is an electron backscatter image of the polished surface. The arrow of the NRM vector contained in the polished surface lies parallel to the (0001) lamellar interfaces.

2.2 Individual crystals versus crystal assemblages

Fig. 3(a) shows the simple geometrical relationships of a single hemo-ilmenite crystal. For a single crystal, the (0001) basal plane is the plane containing the k_1^0 (maximum) and k_2^0 (intermediate) axes of the susceptibility ellipsoid, which is normal to the k_3^0-axis. The vector $\mathbf{n}^0$ denotes the direction of the *c*-axis of the individual crystal in space. In polycrystalline assemblages, a statistical (0001) basal plane is defined by the mean k_1- and k_2-axes and a statistical *c*-axis lies along the k_3 orientation normal to it. Fig. 3(b) shows the geometrical relationships of a polycrystalline assemblage consisting of many crystals with different orientations. Together, the vector $\mathbf{n}$ gives the direction of the statistical *c*-axis in space, and a Fisher parameter K describes the scatter of individual *c*-axes, shown as black points on the top surface of the sphere in Fig. 3(b). In natural samples, the platelet orientations could be systematically folded about an axis parallel to the statistical (0001), with k_1 parallel to the fold axis and the weaker k_2 normal to the fold axis (Siemes *et al.* 2000). Then the *c*-axes distribution is triaxial, and hence,

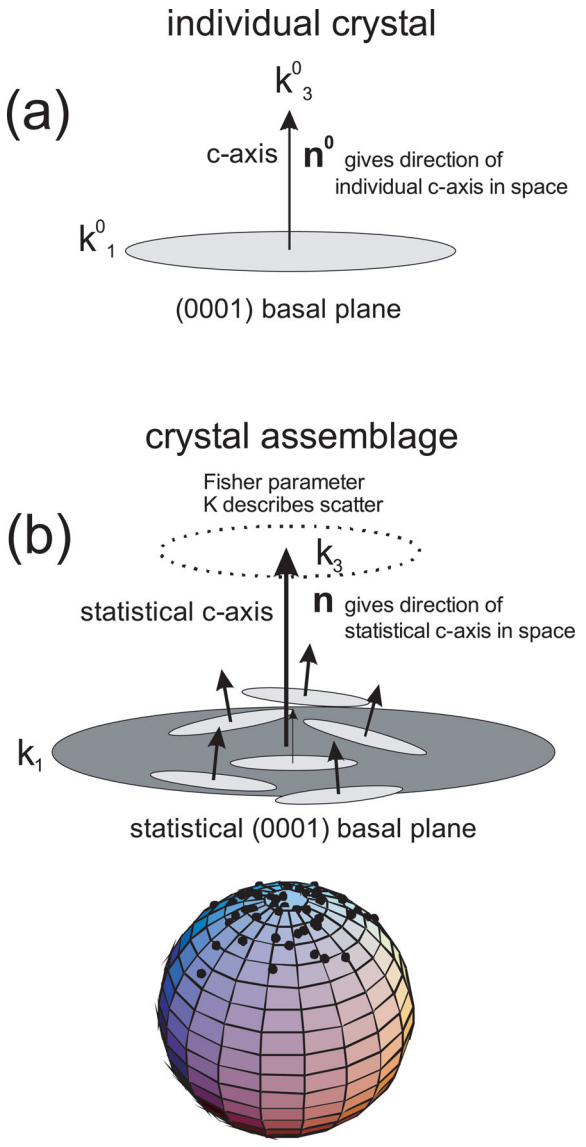

Figure 3. Property relationships in a hemo-ilmenite individual crystal and in a polycrystalline assemblage. (a) Individual crystal with the (0001) basal plane, the crystallographic *c*-axis and the k_1^0- and k_3^0-axes of the AMS. (b) Crystal assemblage with the statistical (0001) basal plane, the statistical crystallographic *c*-axis, and the k_1- and k_3-axes of the AMS.

the AMS ellipsoid is a triaxial ellipsoid, where the susceptibility k_3 would have a higher value. Here, because the observed AMS nearly always has oblate character, it is a good approximation to assume a circular Fisher distribution, where all the k_3^0 attitudes of the illustrated platelets are symmetrically disposed about **n**.

Appendix B considers the possibility that the NRM is constrained crystallographically within the basal plane, destroying circular symmetry, as may be implied in Fig. 2(a). However, it is found that this effect is small and generally averages out in polycrystalline assemblages.

2.3 Unit transformation

Hargraves (1959a) originally reported data in cgs units. Later remeasurements by Hargraves, that he provided to us, and new measurements by McEnroe *et al.* (2007b) in SI units are combined with the remaining historic NRM and AMS values, which were transformed into SI units (see Appendix A). AMS ratio plots are unaffected by units. Table 1 contains Hargraves' NRM and AMS data, either original or transformed. Table 2 contains AMS ellipsoid axial ratios and our own angular measurements derived from orientation data in Table 1.

2.4 NRM intensity compared to magnetic susceptibility

Originally we were concerned about the effect on susceptibility, caused by the presence of minor magnetite in some samples, and about further effects of magnetite on magnetic intensity and anisotropy of susceptibility. However the final analysis showed that for those samples with the highest susceptibility, magnetite contributes little to the anisotropy of the AMS and the NRM. For some samples with intermediate susceptibility, as indicated by the mean value

$$\bar{k} = \frac{k_1 + k_2 + k_3}{3}, \tag{1}$$

there is an increase in AMS (discussed in Section 2.6), but this increase only enhances the AMS in directions entirely compatible with the AMS of polycrystalline hemo-ilmenite. Magnetite has no significant magnetocrystalline anisotropy. Therefore, if a small amount of magnetite enhances AMS, it is likely a shape anisotropy. One possibility is that small amounts of magnetite are distributed between the oriented plates of ilmenite to produce a magnetite shape anisotropy that is parallel to the hemo-ilmenite magneto-crystalline anisotropy. Another possibility, documented in reflected-light images (Fig. 4), is that some ilmenite contains high-temperature reduction-exsolution lamellae of magnetite parallel to (0001) that preceded standard exsolution of hematite from ilmenite, thus enhancing the hemo-ilmenite anisotropy. This texture appears to be related to samples with large amounts of pyrite. Fig. 5 is a plot of NRM intensity (transformed to A m^{-1}) versus magnetic susceptibility as expressed by the $\bar{k}$ of the AMS. Altogether there are only six samples with $\bar{k} > 0.048$ SI and not one has high NRM intensity. Within the samples with lower $\bar{k}$, there are 10 with intensities >90 A m^{-1}. Of these four have $\bar{k} > 0.016$ SI, and the remaining six, all with intensities >100 A m^{-1}, have $\bar{k} < 0.016$ SI. This figure ends speculation that high NRM intensity is related to high susceptibility. To the contrary, samples with the highest NRM's are those with low susceptibility.

2.5 Anisotropy of magnetic susceptibility: anisotropy ellipsoids

Fig. 6 shows the axial ratios of the AMS ellipsoids for all samples on a modified Flinn diagram (Flinn 1962). The ratio k_2/k_3 is the ratio of the intermediate axis to the short axis; the ratio k_1/k_2 is the ratio of the long axis to the intermediate axis. Nearly all of the ellipsoids are oblate, indicating a significant ratio k_2/k_3 in the range of 1.2–4.2, coupled with a small ratio k_1/k_2 ranging from 1 (a perfect oblate spheroid with nine examples) to only slightly less than 1.5. A line at a ratio of 1:1 is the boundary between oblate and prolate fields, and all but two samples plot in the oblate area. These two samples may be examples of the 'folding' described in connection with Fig. 3(b) above.

2.6 Magnetic intensity versus anisotropy of susceptibility

Fig. 7 shows the NRM intensity versus the anisotropy of susceptibility of AMS as expressed by the ratio k_2/k_3 for all samples.

Table 1. Measurements of NRM intensity, declination and inclination, declination and inclination of k_3-axis of the AMS ellipsoid, k_1, k_2, k_3 values of AMS and mean k of the AMS.

Sample	NRM[1]	NRM °Decl.[2]	NRM °Inc.[2]	k_3 °Decl.	k_3 °Incl.	k_1	k_2	k_3	k mean
20c	53.8	339	75	151	25	0.610	0.580	0.440	0.5433
20d	61.6	300	68	160	15	0.480	0.460	0.280	0.4067
21c	50.8	68	22	256	70	0.540	0.390	0.220	0.3833
21d	58.6	72	25	264	65	0.330	0.300	0.140	0.2567
23a	75.3	26	51	240	60	0.089	0.084	0.060	0.0777
23c	81.1	148	54	302	26	0.060	0.060	0.036	0.0520
26b	88.8	125	67	300	00	0.084	0.084	0.046	0.0713
33a	55.7	39	52	201	38	0.196	0.196	0.102	0.1647
33b	46.0	79	57	345	70	0.153	0.153	0.100	0.1353
35an	68.5	327	54	156	69	0.043	0.043	0.025	0.0370
35bn	82.1	330	70	150	55	0.040	0.037	0.024	0.0337
36a	22.5	237	47	0	90	0.035	0.030	0.023	0.0293
36b	32	248	45	0	70	0.037	0.035	0.030	0.0340
46a	27.4	86	62	214	54	0.450	0.390	0.360	0.4000
46b	35.2	90	65	275	36	0.540	0.480	0.400	0.4733
85a	51.8	135	58	0	30	0.350	0.340	0.110	0.2667
85b	61.6	149	57	357	24	0.440	0.430	0.170	0.3467
86a	76.3	23	65	222	32	0.145	0.143	0.069	0.1190
86b	81.2	31	71	239	27	0.100	0.098	0.039	0.0790
90a	48.9	53	35	265	70	1.360	1.200	0.760	1.1067
95c	48.9	147	37	22	48	0.690	0.640	0.340	0.5567
95d	54.7	153	39	20	43	0.500	0.470	0.210	0.3933
96a	53.8	118	24	346	39	0.560	0.540	0.260	0.4533
96b	64.6	134	45	329	41	0.550	0.520	0.230	0.4333
97a	47.9	112	22	0	90	1.240	1.240	0.580	1.0200
97b	46.9	116	19	0	90	1.500	1.390	0.680	1.1900
98a	44.0	131	43	307	59	0.330	0.320	0.175	0.2750
98b	49.8	118	47	304	65	0.348	0.340	0.187	0.2917
105a	37.2	160	27	07	68	0.560	0.560	0.205	0.4417
105b	35.2	149	27	11	62	0.460	0.450	0.190	0.3667
110a	58.6	66	49	217	55	0.536	0.508	0.187	0.4103
110b	58.6	61	49	219	57	0.484	0.460	0.170	0.3713
112a	17.0	144	13	75	70	0.710	0.680	0.198	0.5293
112b	17.6	136	06	Vert.	90	0.740	0.680	0.208	0.5427
114a	39.1	58	42	215	55	0.300	0.260	0.120	0.2267
114b	44.0	70	37	201	58	0.260	0.250	0.091	0.2003
206a	43.0	05	60	230	27	0.248	0.244	0.086	0.1927
206b	44.0	22	62	242	30	0.205	0.199	0.063	0.1557
207a	21.5	107	32	228	42	0.580	0.570	0.244	0.4647
207b	26.9	108	40	228	42	0.560	0.540	0.234	0.4447
210a	45.0	28	51	264	38	0.372	0.302	0.193	0.2890
210b	53.8	28	60	303	17	0.368	0.308	0.100	0.2587
212a	38.1	131	59	01	55	0.230	0.190	0.120	0.1800
212b	31.3	131	59	327	54	0.310	0.260	0.150	0.2400
213a	26.6	116	56	00	65	0.380	0.350	0.207	0.3123
213b	19.7	116	40	00	75	0.375	0.370	0.198	0.3143
214a	86.1	55	79	270	10	0.560	0.540	0.210	0.4367
214b	80.0	57	76	270	0	0.360	0.340	0.175	0.2917
216a	43.1	149	64	38	56	0.098	0.094	0.065	0.0857
216b	46.9	100	69	348	29	0.097	0.094	0.078	0.0+897
216c	44.1	172	80	03	33	0.118	0.115	0.083	0.1053
Le7a	102.8	68	32	235	60	0.030	0.030	0.020	0.0267
Le7b	120.0	53	38	215	65	0.035	0.035	0.024	0.0313
Le64a	72.9.5	98	18	Vert.	90	0.061	0.060	0.044	0.0550
Le64b	77.0	93	10	00	70	0.064	0.062	0.044	0.0567
Le71a	102.8	155	43	276	52	0.040	0.039	0.025	0.0347
Le71b	111.5	143	42	280	58	0.039	0.036	0.021	0.0320
Gr117a	75.4	33	50	245	60	0.122	0.119	0.062	0.1010
Gr117b		33	50	229	44	0.119	0.110	0.043	0.0907
Gr118a	43.0	62	81	0	90	0.412	0.356	0.222	0.3300
Gr118b	31.3	72	74	0	90	0.266	0.216	0.150	0.2107
Gr119a	56.7	272	74	165	10	0.440	0.386	0.135	0.3203
Gr119b	101.8	280	63	170	0	0.296	0.290	0.101	0.2290

Table 1. (*Continued.*)

Sample	NRM[1]	NRM °Decl.[2]	NRM °Inc.[2]	k_3 °Decl.	k_3 °Incl.	k_1	k_2	k_3	k mean
Nwa219a	17.6	161	38	0	90	0.102	0.095	0.060	0.0857
Nwa219b	19.5	177	38	0	90	0.112	0.102	0.076	0.0967
Nwa220a	45.0	241	32	180	0	0.165	0.156	0.062	0.1277
Nwa220b	45.0	243	34	180	0	0.159	0.137	0.061	0.1190
Nwa221a	36.2	115	56	283	39	0.147	0.145	0.035	0.1090
Nwa221b	31.3	116	53	294	40	0.153	0.147	0.037	0.1123
La123a	73.4	124	68	240	7	0.320	0.290	0.195	0.2683
La123b	84.2	126	64	254	26	0.260	0.240	0.180	0.2267
La125a	37.2	90	56	303	40	1.280	1.240	0.830	1.1167
La129c	68.5	195	67	338	13	2.220	2.180	1.060	1.8200
La129d	44.1	162	65	355	14	2.100	2.020	1.060	1.7267
La147a	74.4	111	30	326	68	0.528	0.496	0.380	0.4680
La147b	93.9	117	27	306	65	0.328	0.314	0.178	0.2733
La149a	103.7	154	44	287	29	0.450	0.302	0.208	0.3200
La149b	90.9	137	47	277	50	0.410	0.328	0.209	0.3157
La150a	73.4	164	36	19	58	0.185	0.178	0.081	0.1480
La150b	58.7	163	40	35	66	0.187	0.172	0.095	0.1513
La152a	112.5	212	56	59	40	0.178	0.167	0.112	0.1523
La152b	107.6	221	66	39	50	0.094	0.091	0.065	0.0833

Notes: [1]Hargraves cgs measurements converted to SI, except 36b, Le7b measured by McEnroe, [2]Magnetization vector is shown here in lower hemisphere, but is actually reversed in upper hemisphere except for samples 33an and 33bn which have normal magnetization, [3]k_1, k_2 and k_3 values of the AMS in emu/unit volume, and k mean of these.

Table 2. Axial ratios of the AMS ellipsoids, angles of NRM to statistical (0001) plane of the AMS (ψ), angle of NRM to paleomagnetic vector v (β), angle of statistical (0001) plane to paleomagnetic vector (α) and angle of paleomagnetic vector v to GC containing k_3 of the AMS and the NRM ($\measuredangle(v, GC)$).

Sample	k_1/k_3	k_2/k_3	k_1/k_2	ψ	β	α	$\measuredangle(v, GC)$	Class	Fig. 13
20c	1.39	1.32	1.05	9.8	13.7	22.7	5	B	
20d	1.71	1.64	1.04	−2.2	25.0	11.8	20		
21c	2.45	1.77	1.38	2.3	61.4	63.8	0	B	
21d	2.36	2.14	1.10	0.3	58.4	58.9	1	B	
23a	1.48	1.40	1.06	24.2	32.4	53.0	12	A	
23c	1.67	1.67	1.00	−6.5	38.3	24.1	20		
26b	1.83	1.83	1.00	23.1	22.8	2.1	9	A	(c)
33a	1.92	1.92	1.00	1.3	31.0	32.0	3	A	
33b	1.53	1.53	1.00	50.8	27.4	72.5	11	A	
35an	1.72	1.72	1.00	33.1	35.6	66.0	9	A	
35bn	1.67	1.54	1.08	35.2	19.7	53.4	7	A	(d)
36a	1.52	1.30	1.17	47.0	49.6	83.3	1	A	(f)
36b	1.23	1.17	1.06	35.0	51.4	73.9	15	A	
46a	1.25	1.08	1.15	32.6	22.7	46.8	16		
46b	1.35	1.20	1.13	11.0	20.4	31.0	3	B	
85a	3.18	3.09	1.03	5.2	32.6	34.5	13	B	
85b	2.56	2.53	1.02	−6.0	35.5	28.5	9	B	
86a	2.10	2.07	1.01	8.1	18.7	24.9	8	A	
86b	2.56	2.51	1.02	10.0	12.5	20.3	7	A	(b)
90a	1.79	1.58	1.13	17.6	47.8	64.0	8		
95c	2.03	1.88	1.08	8.0	54.8	54.2	21		
95d	2.38	2.24	1.06	2.5	53.5	49.5	19		
96a	2.15	2.08	1.04	−13.0	64.1	42.4	26		
96b	2.39	2.26	1.06	−2.8	45.2	42.4	1	B	
97a	2.14	2.14	1.00	22.0	65.4	83.3	6		
97b	2.21	2.04	1.08	19.0	68.7	83.3	7		
98a	1.89	1.83	1.03	12.1	47.0	57.4	8	B	
98b	1.86	1.82	1.02	22.0	41.3	62.5	5	B	
105a	2.73	2.73	1.00	7.0	66.1	73.2	2	B	
105b	2.42	2.37	1.02	5.1	64.9	67.6	10	B	
110a	2.87	2.72	1.06	16.8	34.5	48.1	12	B	
110b	2.85	2.71	1.05	17.6	34.2	49.8	9	B	
112a	3.59	3.43	1.04	19.7	78.3	75.7	13	B	
112b	3.56	3.27	1.09	6.0	84.2	83.3	7	B	
114a	2.50	2.17	1.15	8.8	41.2	47.7	11	B	
114b	2.86	2.75	1.04	13.8	46.5	51.4	20		

Table 2. (*Continued.*)

Sample	k_1/k_3	k_2/k_3	k_1/k_2	ψ	β	α	$\measuredangle(v, GC)$	Class	Fig. 13
206a	2.88	2.84	1.02	4.2	25.0	19.8	19		
206b	3.25	3.16	1.03	7.3	21.5	23.0	14	A	
207a	2.38	2.34	1.02	1.8	54.8	34.8	37		
207b	2.39	2.31	1.04	8.4	46.6	34.8	33		
210a	1.93	1.56	1.23	11.6	32.1	31.9	23		
210b	3.68	3.08	1.19	17.3	23.3	15.5	24		
212a	1.92	1.58	1.21	30.0	31.3	59.4	9	B	
212b	2.07	1.73	1.19	23.7	31.3	54.9	2	B	
213a	1.84	1.69	1.09	40.7	32.4	69.6	9	B	
213b	1.89	1.87	1.01	32.8	48.1	79.0	5	B	
214a	2.67	2.57	1.04	0.9	4.4	5.0	2	B	
214b	2.06	1.94	1.06	12.2	7.3	5.5	3	B	
216a	1.51	1.45	1.04	41.3	28.4	63.2	14	A	
216b	1.24	1.21	1.03	20.1	17.9	32.9	11	A	
216c	1.42	1.39	1.03	23.2	15.3	37.7	3	A	
Le 7a	1.50	1.50	1.00	2.5	51.6	53.1	8	A	
Le 7b	1.46	1.46	1.00	13.9	45.2	58.3	7	A	(e)
Le 64a	1.39	1.36	1.02	18.0	68.0	83.3	5	A	
Le 64b	1.45	1.41	1.03	8.3	75.3	74.0	14	A	
Le 71a	1.60	1.56	1.03	17.7	49.9	47.1	31		
Le 71b	1.86	1.71	1.08	16.2	49.3	53.5	22		
Gr117a	1.97	1.92	1.03	22.8	32.8	53.3	11	A	
Gr117b	2.77	2.56	1.08	5.2	32.8	36.9	8	A	
Gr118a	1.86	1.60	1.16	80.9	3.1	83.3	2	B	
Gr118b	1.77	1.44	1.23	73.8	10.2	83.3	3	B	
Gr119a	3.26	2.86	1.14	4.8	21.4	6.2	21		
Gr119b	2.93	2.87	1.02	8.8	32.0	3.9	31		
Nwa219a	1.70	1.58	1.07	38.0	55.4	83.3	6	A	
Nwa219b	1.47	1.34	1.10	38.0	56.8	83.3	5	A	
Nwa220a	2.66	2.52	1.06	− 24.6	65.0	3.3	59		
Nwa220b	2.61	2.25	1.16	− 22.3	62.8	4.7	57		
Nwa221a	4.20	4.14	1.01	6.1	32.2	35.1	11	A	
Nwa221b	4.14	3.97	1.04	3.5	35.3	37.2	7	A	(a)
La123a	1.64	1.49	1.10	3.0	21.5	0.0	21		
La123b	1.44	1.33	1.08	8.5	25.1	19.6	22		
La125a	1.54	1.49	1.03	10.2	29.2	38.3	8		
La129c	2.09	2.06	1.02	− 5.3	29.0	15.4	19		
La129d	1.98	1.91	1.04	− 10.7	29.0	18.3	0		
La147a	1.39	1.31	1.06	11.5	57.4	68.3	4	B	
La147b	1.84	1.76	1.04	2.1	61.1	63.0	3	B	
La149a	2.16	1.45	1.49	− 5.4	48.6	25.3	34		
La149b	1.96	1.57	1.25	12.9	43.8	45.4	10	B	
La150a	2.28	2.20	1.04	8.6	57.7	64.5	9	A	
La150b	1.97	1.81	1.09	23.2	53.6	73.0	10	A	
La152a	1.59	1.49	1.07	8.6	41.1	47.2	12	A	
La152b	1.45	1.40	1.03	26.2	31.3	57.2	2	A	

Note: AMS anisotropy, k_1/k_3 = ratio of long to short axis of AMS ellipsoid, k_2/k_3 =ratio of intermediate to short axis and k_1/k_2 = ratio long to intermediate axis.

Grey shading indicates the more limited range of values for 55 samples after quality assessment. Note that for AMS values below 1.2, NRM's are not very strong, but there is a rapid increase in intensity reaching a maximum at k_2/k_3 values of only 1.4–1.5, after which, with rare exceptions, intensity falls with rising AMS, and the seven samples with $k_2/k_3 > 3$ have low intensities. This figure supports statements by Hargraves (1959b, p. 1575) that NRM intensity in the Lac Tio samples is mainly a function of orientation of the statistical (0001) basal planes with respect to the magnetizing field and that it is not a function of degree of LPO as concluded by Carmichael (1959).

2.7 Magnetic anisotropy versus magnetic susceptibility

Fig. 8 shows magnetic anisotropy expressed as k_2/k_3 plotted against susceptibility $\bar{k}$. Samples with very low susceptibility with $\bar{k} < 8 \times 10^{-3}$ SI (8 mSI) also have low anisotropy below 2. For susceptibilities $\bar{k}$ from 8 to 48 mSI, many anisotropies are in the range of 2–3.4, with 2 at 4–4.2. There are six samples with $\bar{k} > 48$ mSI and the highest anisotropy among these is 2.2. High anisotropy is most common with intermediate susceptibility samples, and does not occur with very high, or very low susceptibility samples. The data indicate that a small amount of magnetite may actually

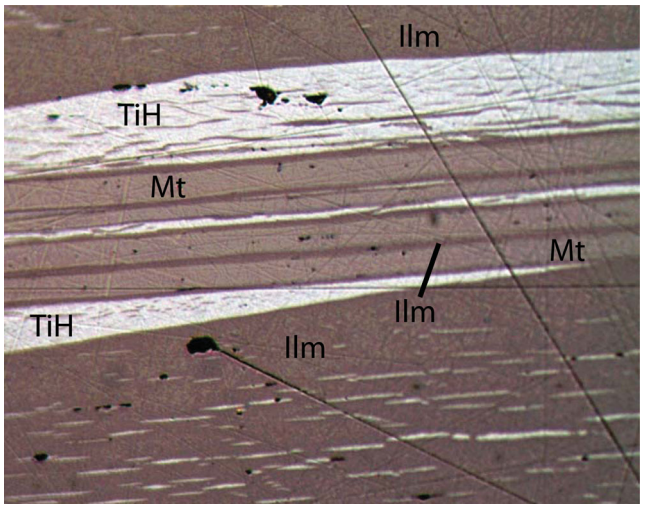

Figure 4. Reflected-light photomicrograph of Allard Lake hemo-ilmenite showing lamellae of magnetite (intermediate reflectance) accompanying coarse titanohematite exsolution lamellae (bright reflectance) parallel to (0001) of the ilmenite host (dark reflectance). Hematite and ilmenite show fine exsolutions parallel to (0001) lacked by the magnetite. A magnetic shape anisotropy of the lamellae of magnetite can be added to the magneto-crystalline anisotropy of hemo-ilmenite in samples with an intermediate susceptibility indicative of a small amount of magnetite. Textural relationships suggest the magnetite likely formed during an early, localized, reduction-exsolution, followed at lower temperature by normal exsolution of coarse hematite, then mutual fine exsolution at still lower temperature. Hargraves noted that magnetite was commonly associated with pyrite in these samples.

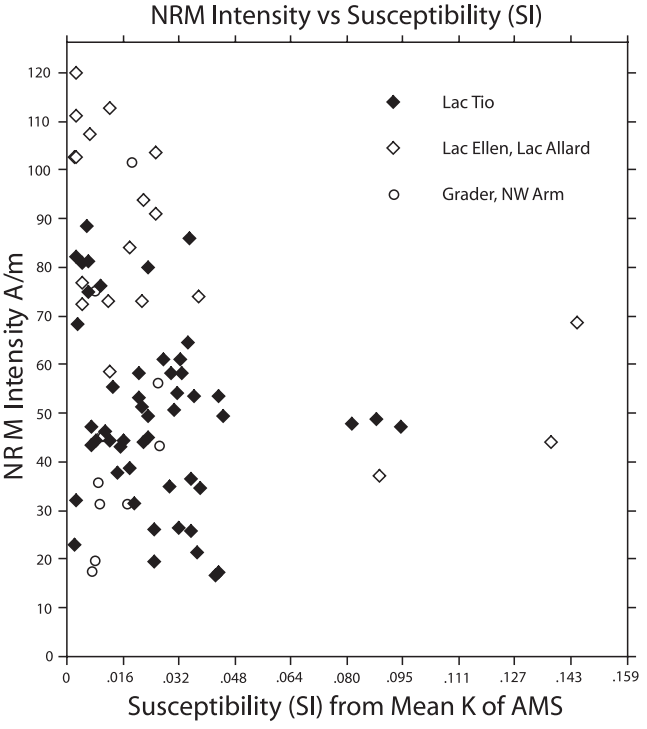

Figure 5. NRM intensity in A m^{-1} versus susceptibility derived from the mean $\bar{k}$ of the AMS.

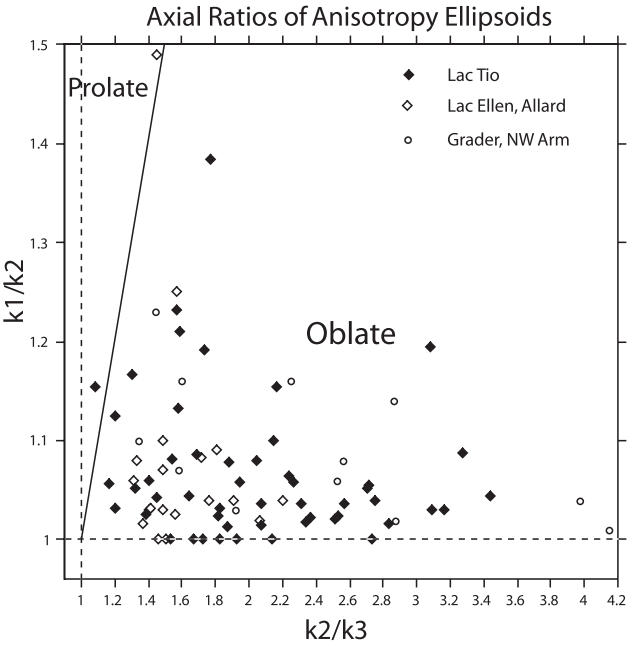

Figure 6. k_1/k_2 versus k_2/k_3, which are the axial ratios of the AMS ellipsoid. Diagram is modified from the diagram of Flinn (1962) .

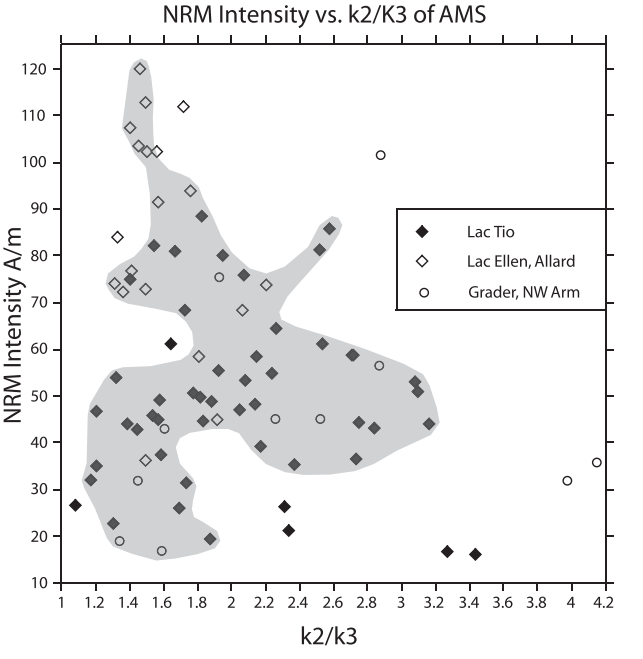

Figure 7. Intensity of NRM in A m^{-1} (SI) versus anisotropy of the AMS expressed as k_2/k_3. Grey shading indicates the slightly more restricted range covered by the best 55 samples in groups A and B following quality assessment (see Section 3.5).

enhance magnetic anisotropy of polycrystalline assemblages of hemo-ilmenite.

3 CRYSTAL ASSEMBLAGE PROPERTIES RELATIVE TO MAGNETIZING FIELD

3.1 General features

To here we have considered solely intrinsic properties of individual samples. Now we also include properties related to the orientation

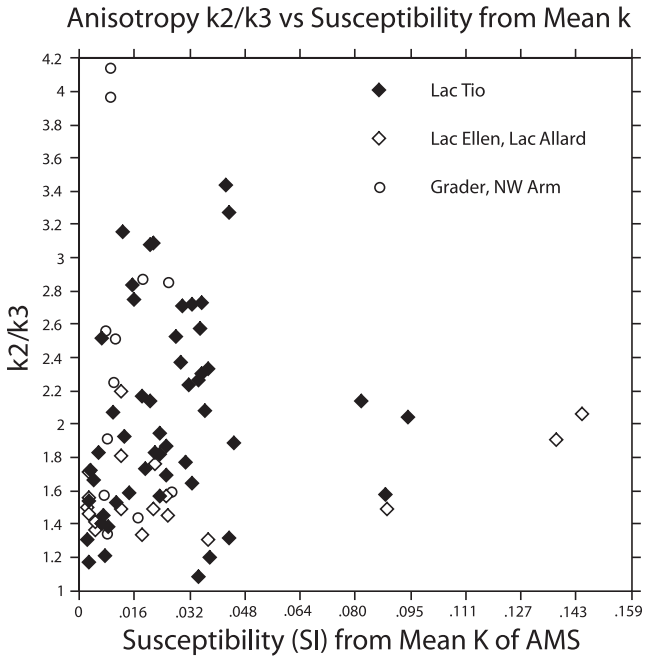

Figure 8. Magnetic anisotropy as expressed by k_2/k_3 versus magnetic susceptibility represented by $\bar{k}$ of k_1, k_2, k_3 of the AMS.

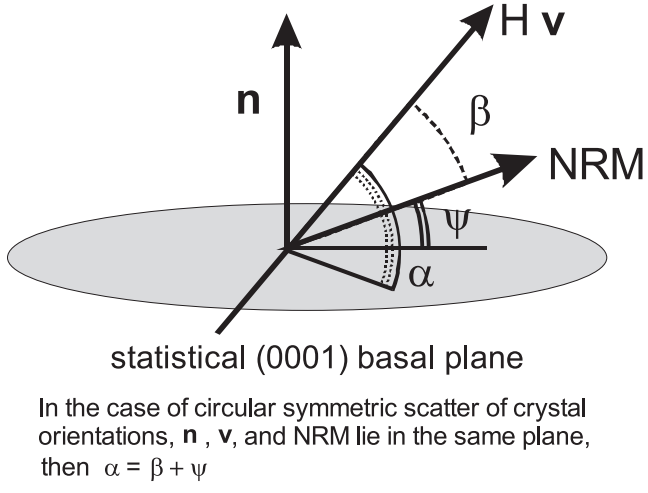

Figure 9. Relationships between angular properties inherent in an assemblage of hemo-ilmenite crystals and the magnetizing field that created the magnetization during exsolution.

of the external magnetizing field at the time the lamellae were magnetized. Fig. 9 shows geometrical relationships. The grey plane is the statistical (0001) basal plane of the assemblage, as determined by the $k_1 - k_2$ plane of the AMS, or by a plane normal to the k_3-axis. The vector **n** represents the orientation of the statistical *c*-crystallographic axis of the assemblage, here determined by the k_3-axis of the AMS. The angle ψ represents the deviation of the NRM from the statistical (0001) basal plane of the assemblage. It is related to the orientation of the magnetizing field, represented by the unit vector **v**, and its intensity H, during the magnetization process with respect to the statistical basal plane, as shown in Fig. 10. The vector **v** is at the angle α to the basal plane, and at the angle β to the NRM. Theoretically, if the crystal assemblage has circular symmetric scatter (an oblate spheroid), which would be indicated in the AMS by $k_1 = k_2 (k_1/k_2 = 1.00)$, then **n** (indicated by k_3), **v** and the NRM vector lie on the same great circle (GC) so that $\alpha = \beta + \psi$. If $k_1 > k_2$ so that $k_1/k_2 > 1$, indicating a triaxial AMS ellipsoid, then it is possible that **v** will not lie on the GC connecting k_3-axis and the NRM (see Appendix B). In natural samples, such a discrepancy could also be due to sample misorientation, measurement error, or to an error in the determination of the magnetizing field **v**. Thus, a measure of the angle $\measuredangle(\mathbf{v}, GC)$ (Table 2) is a useful indicator of how well results fulfill ideal relationships.

The deviation angle ψ of the NRM from the statistical (0001) basal plane is also related to the strength of the LPO as expressed by k_2/k_3, being smallest for a strong LPO and largest for a weak LPO (see Fig. 11 below). Some samples show a deviation angle ψ that is in the opposite direction with respect to the basal plane from the direction of the magnetizing field, **v**. In these cases, ψ is expressed as a negative angle in Table 2. Such results, not compatible with theory, are likely due to sample misorientation, or measuring errors. However, in situations where the magnetizing field **v** is nearly parallel to the (0001) basal plane and/or where the k_2/k_3 anisotropy is large, a small negative deviation could be a result of only very minor discrepancies between k_3 and NRM measurements. Such samples do not constitute a significant violation of the concepts presented here. Although the magnetizing field is not an inherent property of the crystal assemblage, the orientation of the NRM in each sample is a product of the field orientation **v**.

3.2 A simple model for a crystal assemblage of fixed LPO

Before deriving a more abstract mathematical description based on Fisher statistics in Appendix C, Fig. 10 deduces a conceptual diagram from calculated values of $\beta = \measuredangle(NRM, \mathbf{v})$, NRM intensity and deviation ψ of the NRM from the statistical (0001) basal plane for a fixed LPO and variable orientation of the statistical (0001) basal plane to the magnetizing field. Part A shows a model arrangement of 24 crystals, 12 of which are parallel to the statistical mean and six each are 15° either side of the mean. Each crystal has a synthetic NRM related to its angle to the magnetizing field (large vertical arrows) and proportional to the cosine of the angle between its (0001) basal plane and the magnetizing field, from a value of 1 at 0° to a value of 0 at 90°. The small vectors indicate the mean intensities, and values of NRM intensity,α, β and ψ are listed below each model. Part B consists of graphs showing values of β, NRM intensity and ψ for varying values of α from 0° to 90°, including results for the seven models in part A.

The following insights can be obtained from Fig. 10. As the angle α of the statistical (0001) basal plane to the magnetizing field increases, the angle β of the NRM to the statistical basal plane also increases steadily to a maximum value of 68° for $\alpha = 80°$, then drops sharply to zero by $\alpha = 90°$. Theoretical considerations in Appendix C show that the peak of β is larger and later for strong LPO's, as in this example, and smaller and earlier for weaker LPO's. As the angle α increases, the intensity of NRM declines slowly, then more rapidly, then slowly again as α approaches 90°. The steepness of the intensity curve in the centre is related to the LPO strength such that a sample with no LPO would be represented by a horizontal straight line. As α increases, the angle ψ between NRM and the statistical basal plane increases slowly, and only reaches 7.4° at $\alpha = 75°$, but accelerates rapidly from $\alpha = 80°$ on. For samples with a weaker LPO, the increase in ψ is more rapid earlier, and reaches fairly high values earlier, but still is not close 90° until α itself nearly reaches 90°.

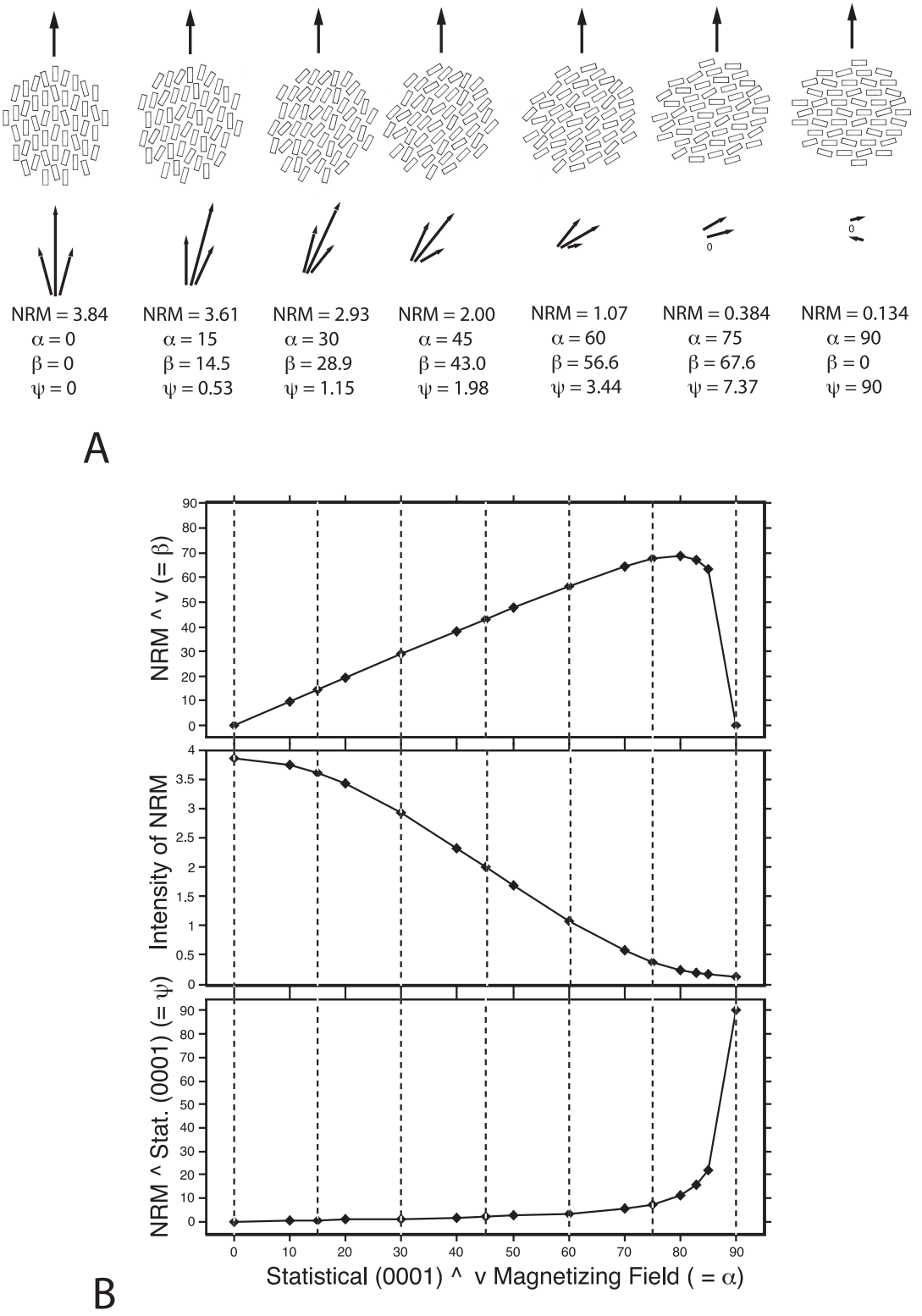

Figure 10. Conceptual diagram based on calculated values of $\beta = \measuredangle(NRM, \mathbf{v})$, NRM intensity and deviation ψ of the NRM from the statistical (0001) basal plane for a fixed LPO and variable orientation of the statistical (0001) basal plane to the magnetizing field.

3.3 Deviation of the NRM from statistical (0001) versus anisotropy

Fig. 11 shows the deviation angle ψ of the NRM from the statistical (0001) basal plane $\measuredangle(NRM, (0001))$ versus anisotropy of the AMS represented by k_2/k_3 for all data, including 10 samples, perhaps in part poorly oriented in the field, with negative angles. Grey shading indicates the more limited range of values for 55 samples after quality assessment, where only two show $\psi < 0$. Unlike Fig. 10, based on a fixed hypothetical anisotropy, this shows samples with a large

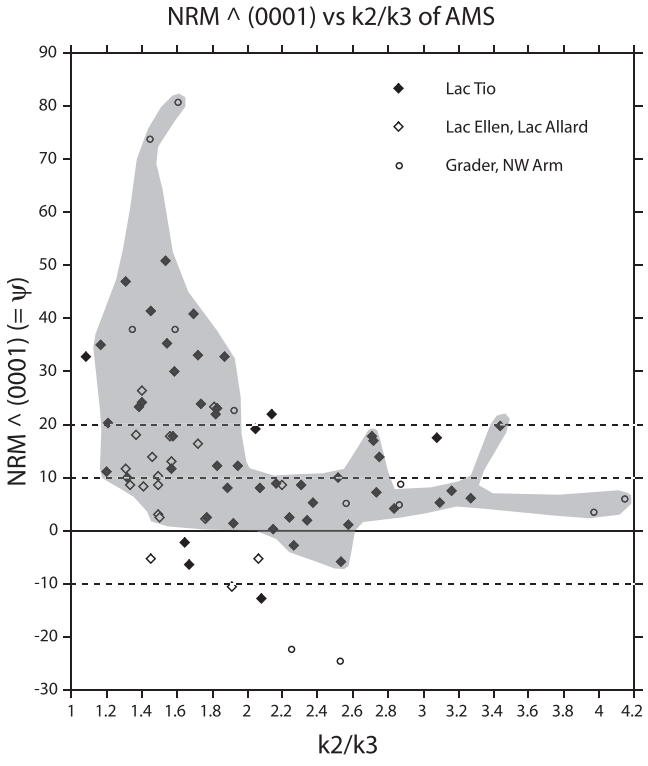

Figure 11. Deviation ψ of the NRM from the statistical basal plane versus anisotropy k_2/k_3. Grey shading indicates the more restricted range covered by the best 55 samples in groups A and B following quality assessment (see Section 3.5).

range of anisotropy. As predicted, samples with high anisotropies do not have large deviations, and no sample with $k_2/k_3 > 2.2$ has a deviation greater than 20°. Highest deviations commonly 40°–50° and in two samples 73° and 80° are recorded for samples with k_2/k_3 from 1.3 to 1.7.

3.4 Finding the orientation of the magnetizing field

The method used by Hargraves (1959a) was to find the GC normal to the statistical (0001) basal plane also containing the NRM. He then postulated that the statistical magnetizing field should lie at the location with the highest density of intersections of these GCs.

Hargraves (1959a) located the statistical peak of intersections for 49 Lac Tio hemo-ilmenite specimens at declination 73° and inclination 72° in the lower hemisphere. Later, using a more mathematical approach, Hargraves & Burt (1967) determined a local field vector for the same specimens with declination 47.9° and inclination 83.3°. We used this value for all our subsequent angular measurements. To give the flavour of the Hargraves (1959a) graphical approach, Fig. 12(a) shows the poles to the same GCs that we determined independently in our evaluation of all 80 samples, excluding the two with normal polarity. In Fig. 12(b) all GCs are plotted with their 3160 intersections. We used the program *cylindrical best fit*, which creates a statistical triaxial ellipsoid based on the poles to the GCs. For this example, the lengths and the declinations and inclinations for the axes of the ellipsoid based on a unit sphere are: L 0.5001, Decl. 202.2°, Incl. 2.0°; L 0.4247, Decl. 292.3°, Incl. 2.5°: L 0.0752, Decl. 74.0°, Incl. 86.8°. The three ellipsoid axes are indicated by shaded squares in Fig. 12(a). The location of the maximum abundance of GC intersections (*Beta*) should lie at the location of

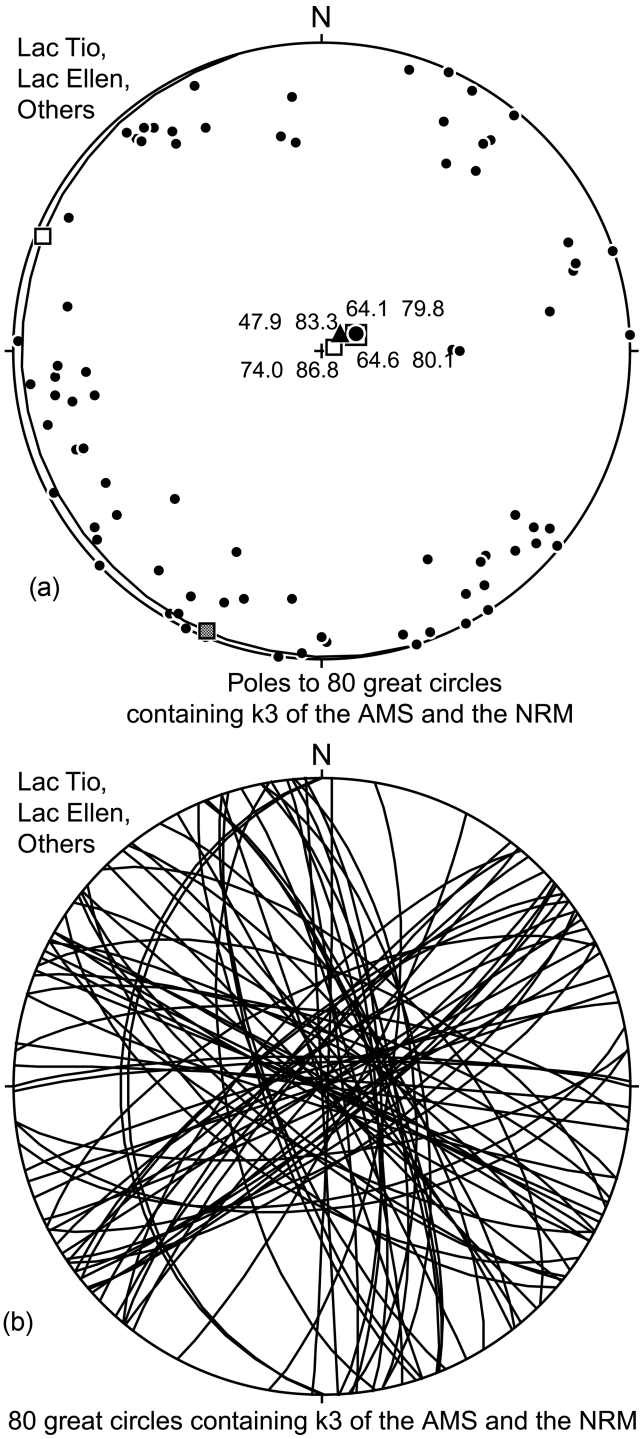

Figure 12. Graphically locating the magnetizing field. (a) Poles to 80 GCs containing k_3 [pole to the statistical (0001) basal plane] and the NRM, excluding two with normal polarity. Also shown are the three axes of a *cylindrical best fit* ellipsoid. The minimum axis of this, at 74.0°, 86.8°, approximates the inverted Mesoproterozoic magnetizing field (closed triangle) at 47.9°, 83.3°, estimated by Hargraves & Burt (1967), using their cross-product technique, on 49 Lac Tio hemo-ilmenite specimens. Also shown is our *cylindrical best fit minimum axis*, (closed circle) at 64.1°, 79.8°, for the same 49 Lac Tio hemo-ilmenite specimens, and the R.M. vector (open square) at 64.6°, 80.1, determined by Hargraves & Burt (1967) for 21 Lac Tio anorthosite samples. (b) All 80 GCs plotted directly, illustrating their 3160 intersections.

the minimum of locations of poles to the GCs, in this case at the ellipsoid axis with declination 74.0°, inclination 86.8°. Although this value appears numerically very different from the value 47.9° and 83.3° of Hargraves & Burt (1967), it differs from the later by only 4°, even though the input is different. When we applied *cylindrical best fit* to the same 49 Lac Tio hemo-ilmenite specimens, we obtained a direction 64.1°, 79.8°. This is identical to a conventional remanent magnetic vector at 64.6°, 80.1° determined by Hargraves & Burt (1967) for 21 Lac Tio ilmeno-hematite-bearing anorthosite samples, providing good support for the basic assumptions.

3.5 Assessment of sample quality

Earlier we indicated that in an ideal crystal assemblage with the LPO of an oblate spheroid, the magnetizing field **v** should lie on a GC containing k_3, the pole to the statistical basal plane, and the NRM (see Appendix B).

We have measured the angle that **v** makes with the GC ($\measuredangle(\mathbf{v}, GC)$) and have used this angle as one means of sample classification. The angle $\measuredangle(\mathbf{v}, GC)$ was plotted against anisotropy k_2/k_3. The effects of AMS ellipsoids with significant triaxial character and likely error in sample orientation or measurement were assessed. The angle $\measuredangle(\mathbf{v}, GC)$ was also plotted against susceptibility $\bar{k}$. The value of $\bar{k}$ can be used to estimate volume concentration $c_{\rm mt}$ of magnetite as

$$c_{\rm mt} \approx \frac{\bar{k} - k_{\rm hi}}{k_{\rm mt}}, \tag{2}$$

where $k_{\rm hi}$ and $k_{\rm mt}$ are the magnetic susceptibilities of pure hemo-ilmenite and magnetite, respectively. Using the approximative values $k_{\rm hi} \approx 0.007$ SI and $k_{\rm mt} \approx 3$ SI, we obtain estimates for $c_{\rm mt}$ which are sufficient for classification of the samples but still contain minor error sources (e.g. minor silica content of the ore sample). Six samples show susceptibilities implying magnetite concentrations $c_{\rm mt} > 2$ per cent. Because we are most interested in examining the behaviour of samples dominated by the lamellar magnetism of hemo-ilmenite with minor or no magnetite, we used this figure to delineate samples with low $\measuredangle(\mathbf{v}, GC) < 15$ and susceptibility implying low $c_{\rm mt}$. For $\measuredangle(\mathbf{v}, GC)$, we have used a natural break at 15°. For susceptibility, we made two selections. A more stringent group A has 28 samples, of which 17 have $\bar{k} < 8$ mSI implying $0 \leq c_{\rm mt} \leq 0.025$ per cent, and the remaining 11 have 8 mSI $< \bar{k} <$ 13.5 mSI giving a maximum $c_{\rm mt}$ of 0.2 per cent. A broader group B of 27 samples has 13.5 mSI $< \bar{k} <$ 44 mSI implying $0.2 < c_{\rm mt} < 1$ per cent. The group selections are listed in Table 2 and the groupings A and A+B are used for more selective plots in several figures.

3.6 Equal area diagrams of selected samples

The above numerical discussion of sample features is best visualized by examining equal area diagrams of the relationships in individual samples. Six of an original 25 diagrams are shown in Fig. 13. They illustrate routine features, and some of the problems of interpretation. Each has $\measuredangle(\mathbf{v}, GC)$ with low susceptibility in group A or B. The six diagrams are arranged in order of decreasing k_2/k_3.

3.7 Plots of properties following quality selection

For the samples in group A, magnetite plays essentially *no* role. Group B samples contain minor magnetite, but we believe that magnetite does not confuse their AMS relationships, and does not notably influence NRM intensity. Fig. 14 shows the angle β of the NRM to the magnetizing field **v** versus the angle α between the statistical (0001) basal plane and **v** for samples in combined groups A + B. This diagram is exactly parallel to Fig. 10(b), part 1. The angle β is theoretically zero in samples with no anisotropy. For samples with high anisotropy and angles α of 70°–80°, it reaches a maximum, but then again drops to 0° at $\alpha = 90°$. It was the effect of this angle that required Hargraves (1959a) to make his constructions to determine the declination and inclination of the magnetizing field.

The two parts of Fig. 15 show NRM intensity versus α, exactly in parallel with Fig. 1, and also Fig. 10(b), part 2. Fig. 15(a) only shows the more stringent selection group A, while Fig. 15(b) includes the broader range of groups A and B. In both parts, the Lac Tio samples show a distinctive negative slope, but with the two normal-polarity samples 35aN and 35bN as outliers on the upper intensity side. Compared with Lac Tio, the Lac Ellen and Lac Allard samples have much higher intensities. We believe that this is due to either composition, or cooling history. None of the Lac Ellen–Lac Allard group has a value of α less than 45°, so one of our objectives is to evaluate the potential magnetic intensity for similar crystal assemblages oriented more favourably with respect to the magnetizing field. The theoretical calculations in Appendix C allow estimation of NRM intensity for any value of α.

The two parts of Fig. 16 show deviation ψ of the NRM from the statistical (0001) basal plane versus α. Fig. 16(a) is for the more stringent selection (group A), while Fig. 16(b) is for the broader range (groups A +B). When the angle α is large, then the capability to pull the NRM away from the basal plane is large, giving a significant angle ψ, especially for low anisotropy k_2/k_3. When the angle α is small, then the capability to pull the NRM away from the basal plane is small, giving a small angle ψ, especially for large $k_2/k_3 > 1$. The solid diagonal line in both parts illustrates the general limit of deviation ψ for varied α in samples from the Lac Tio deposit. One sample (26b) in Fig. 16(a) and two in Fig. 16(b) violate this limit. The problem of sample 26b has already been illustrated in Fig. 13. Note that the deviation limit for Lac Tio samples is seriously exceeded by GR118a and GR118b, which have moderate susceptibility, low anisotropy and low to intermediate NRM intensity.

4 NRM AND AMS OF A FISHER-DISTRIBUTED ASSEMBLY OF PLATELETS

We have investigated theoretical considerations needed to develop a quantitative understanding of the connections between (1) the AMS of the individual crystals, $\sigma^0 = k_3^0/k_1^0$, (2) the AMS of the natural crystal assemblages, $\sigma = k_3/k_1$, (3) the NRM deflection angle β with respect to the external field and (4) the NRM deflection angle ψ from the (0001) basal plane. These considerations, with development of a series of equations, relating these properties to Fisher distributions (K) of orientations of individual crystal platelets, are presented separately in Appendix C. The results, highly pertinent to our overall study, are then applied to create graphic interpretations of relationships in Section 6.

5 FISHER DISTRIBUTION OF *C*-AXES COMPARED TO AMS

In Appendix C, we showed that there is a correlation between the Fisher distribution K of c-crystallographic axes in a crystal assemblage and the magnetic anisotropy of individual crystals. The deviation angle ψ is a function of K in Appendix C (Fig. C3), and it is also a function of k_2/k_3 (or k_1/k_3 for circular distributions) as

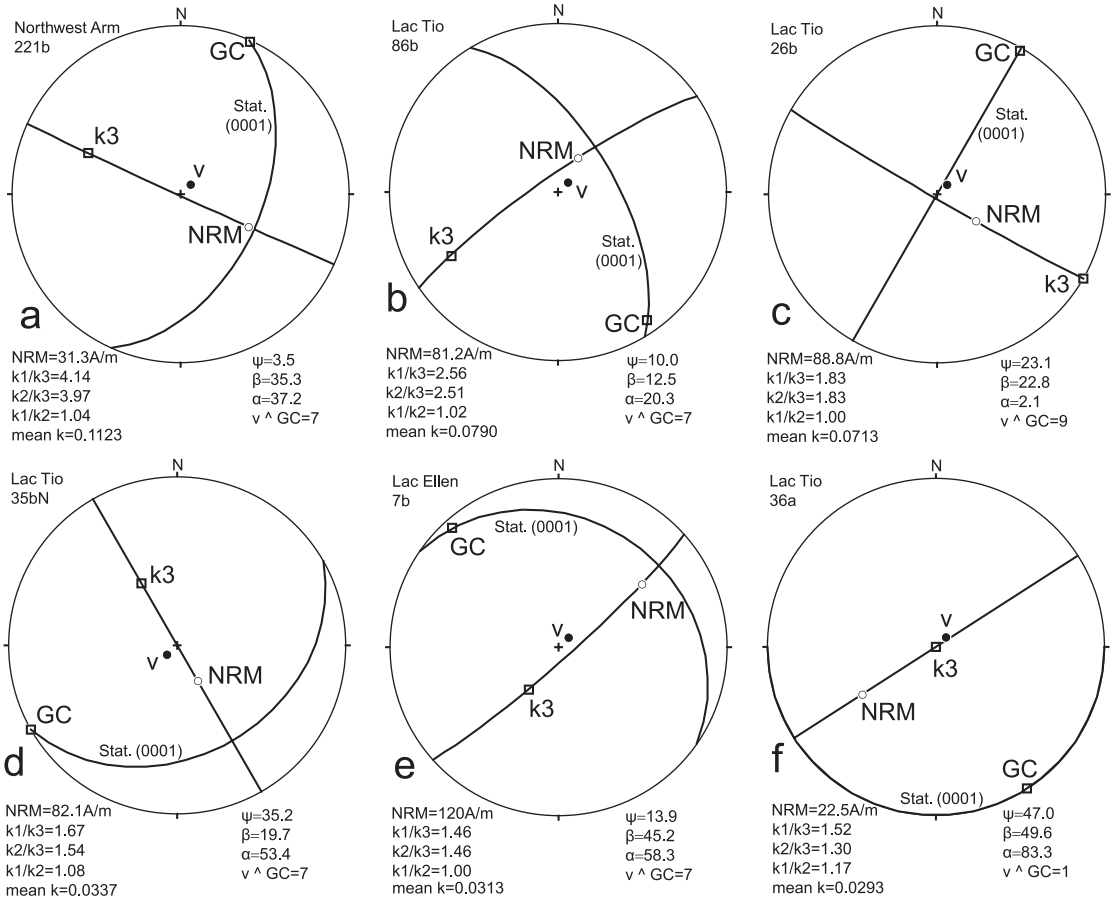

Figure 13. Selected equal area diagrams. (a) Sample Nwa221b with $\measuredangle(\mathbf{v}, GC) = 7^\circ$. High anisotropy $k_2/k_3 = 3.97$ keeps the NRM close to (0001) ($\psi = 3.5^\circ$) even though $\alpha = 37.2^\circ$ is quite large. NRM of 31.3 A m^{-1} is typical of the NW Arm Group (Fig. 15 a). (b) Sample 86b with $\measuredangle(\mathbf{v}, GC) = 7^\circ$ has high $k_2/k_3 = 2.51$ and very low $\bar{k} = 0.079$ in group A. The NRM is very high (81.2 A m^{-1}) and well out of the basal plane ($\psi = 10.0^\circ$) even though α is only 20.3°. (c) Sample26b with $\measuredangle(\mathbf{v}, GC) = 9^\circ$ has moderate $k_2/k_3 = 1.83$ and low $\bar{k} = 0.071$. NRM of 88.8 A m^{-1} is strongest in the Lac Tio group and quite far from (0001) with $\psi = 23.1^\circ$, much larger than $\alpha = 2.1^\circ$, yielding an unexplained anomaly in Fig. 16(a). (d) Sample 35bN with $\measuredangle(\mathbf{v}, GC) = 7^\circ$ has normal polarity (here plotted on upper hemisphere) and was collected about 9 inches from a cross-cutting pegmatite dike. It has fairly low $k_2/k_3 = 1.54$ and very low $\bar{k} = 0.034$. NRM is $\psi = 35.2^\circ$ from (0001), consistent with $\alpha = 53.4^\circ$ and low k_2/k_3 (Fig. 11). The comparatively high NRM at 82.1 A m^{-1} and results for companion sample 35aN suggest that a warming and cooling event, associated with the pegmatite intrusion, provided a thermal window for added exsolution in a normal magnetic field and development of this stronger NRM. Because of the very low susceptibility, this normal overprint is not associated with magnetite. (e) Sample Le7b with $\measuredangle(\mathbf{v}, GC) = 7^\circ$ has low $k_2/k_3 = 1.46$ and very low $\bar{k} = 0.031$. Its NRM is fairly close to (0001) with $\psi = 13.9^\circ$ for $\alpha = 58.3^\circ$ (Fig. 16 a). Typically ψ is lower for the Lac Ellen–Lac Allard samples. The NRM at 120 A m^{-1} is the highest reported here, even though α is large. The large NRM is consistent with other Lac Ellen–Lac Allard Group samples, implying strong lamellar magnetism. Our model predicts that for small α, these samples might have acquired NRM's over 200 A m^{-1}. (f) Sample 36a with $\measuredangle(\mathbf{v}, GC) = 1^\circ$ has low anisotropy $k_2/k_3 = 1.30$ and very low susceptibility $\bar{k} = 0.029$. The NRM is $\psi = 47.0^\circ$ from (0001), consistent with $\alpha = 83.3^\circ$ and with the low anisotropy (Fig. 7). The NRM at 22.5 A m^{-1} is at the lower right end of the envelope (Figs 15 a and b) for ordinary samples from the Lac Tio Group.

in Fig. 11. An important outcome of these comparisons is to show that the ratio k_1^0/k_3^0 of individual crystals is not large. A consequence of this is that a low anisotropy of the AMS can reflect a very strong Fisher distribution of *c*-axes. We have made a test of this by measuring the real distribution of *c*-axis orientations in samples Le7b and 36b by EBSD, and then calculating the AMS from these distributions using the single-crystal AMS data provided by single crystal #19 extracted from sample 36b. The details of this aspect of the study are presented separately in Appendix D.

6 EXTRAPOLATED PROPERTIES OF NATURAL CRYSTAL ASSEMBLAGES

Using the equations in Appendix C, relating NRM and the AMS of generic assemblages of hemo-ilmenite platelets, it is possible to calculate properties of given assemblages of platelets based on selected samples, where the properties change as a result of a different angle α of the statistical (0001) basal plane to the magnetizing field v. The properties we have chosen to calculate are β, the angle the NRM makes with the magnetizing field **v** (Fig. 17); the NRM intensity in A m^{-1} (Fig. 18); and ψ, the angular deviation of the NRM from the statistical (0001) basal plane (Fig. 19).

By selecting samples showing the best angular relationships and the lowest susceptibility, we focus on the hemo-ilmenite lamellar magnetism. The resulting curves were calculated using the function y that derives from ψ and α according to eq. (C10) in Appendix C. Values of ψ and α and calculations of y are given in Table E2 of Appendix D.

Values of y and curves in Figs 17–19 are independent of the measurements of AMS except to the extent that AMS was used to determine the location of the statistical (0001) basal plane. The

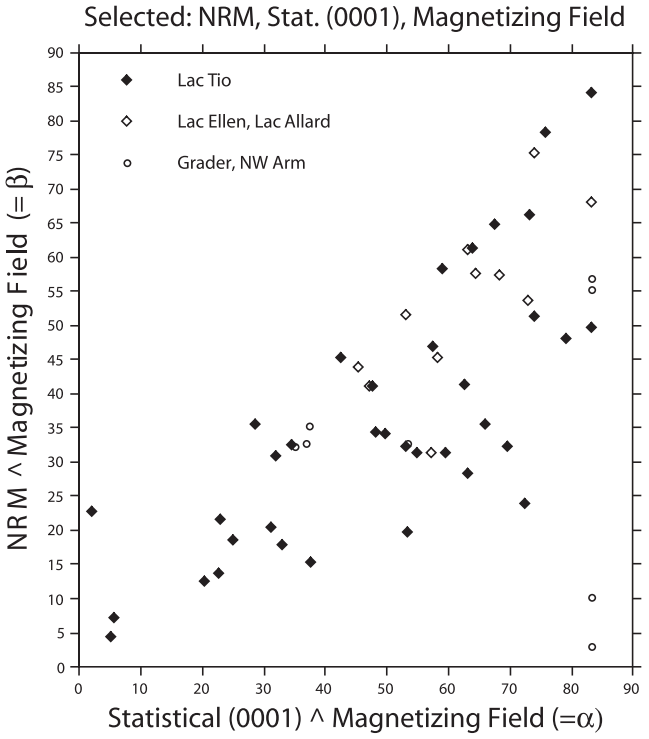

Figure 14. Plot of the angle β from the NRM to the magnetizing field **v** versus the angle α of the statistical (0001) basal plane to **v**. This plot is parallel in concept to Fig. 10(b), part 1.

relationship of the results to the Fisher parameter K is discussed in Appendix C with related Fig. C1, and K can be calculated for individual values of y as illustrated in Fig. C2.

For the collection from the Lac Tio Deposit, there is a wide range in initial values of β, NRM and ψ for different values of α. We chose four samples, 33a, 35aN, 86a and 36b. Much is known in detail about sample 36b (McEnroe *et al.* 2007b), including recently acquired EBSD data reported in Appendix D. The collection from the Lac Ellen–Lac Allard deposits is more limited in number, and in spread of values. However, the available data show that the Lac Ellen–Lac Allard samples have consistently low susceptibility and strong NRM. We attribute the high NRM to more favourable conditions for the development of strong lamellar magnetism, probably related to slightly different cooling conditions that produced abundant very fine exsolution lamellae of ilmenite within large primary hematite exsolution lamellae. For this group, we chose samples Le64b, Le7a, Le7b, La152a and La152b. Sample Le7b has the very strongest NRM, and the new EBSD data on it can be tied to the AMS results as in Fig. D1 of Appendix D. Finally, we selected sample Nwa221b from the weakly magnetic Northwest Arm Group.

Fig. 17 shows extrapolations of β against α. The graphical arrangement is based on part 1 of Fig. 10(b) and on Fig. C3 in Appendix C, and the plot of data points in Fig. 14. From Fig. 10(b) and Fig. C3 in Appendix C, it can be seen that the value of β must be 0 for $\alpha = 0$ and $\alpha = 90^\circ$, but the trajectory follows low values when the Fisher distribution K is weak, and high values when it is strong. Table E2 shows values of K representing each sample and the trajectory upon which it lies in Fig. 17. This figure contains the justification for the method used by Hargraves (1959a) to locate the Proterozoic magnetizing field.

Fig. 18 shows extrapolations of NRM intensity in A m^{-1} against α. The graphical arrangement is based on part 2 of Fig. 10(b), and

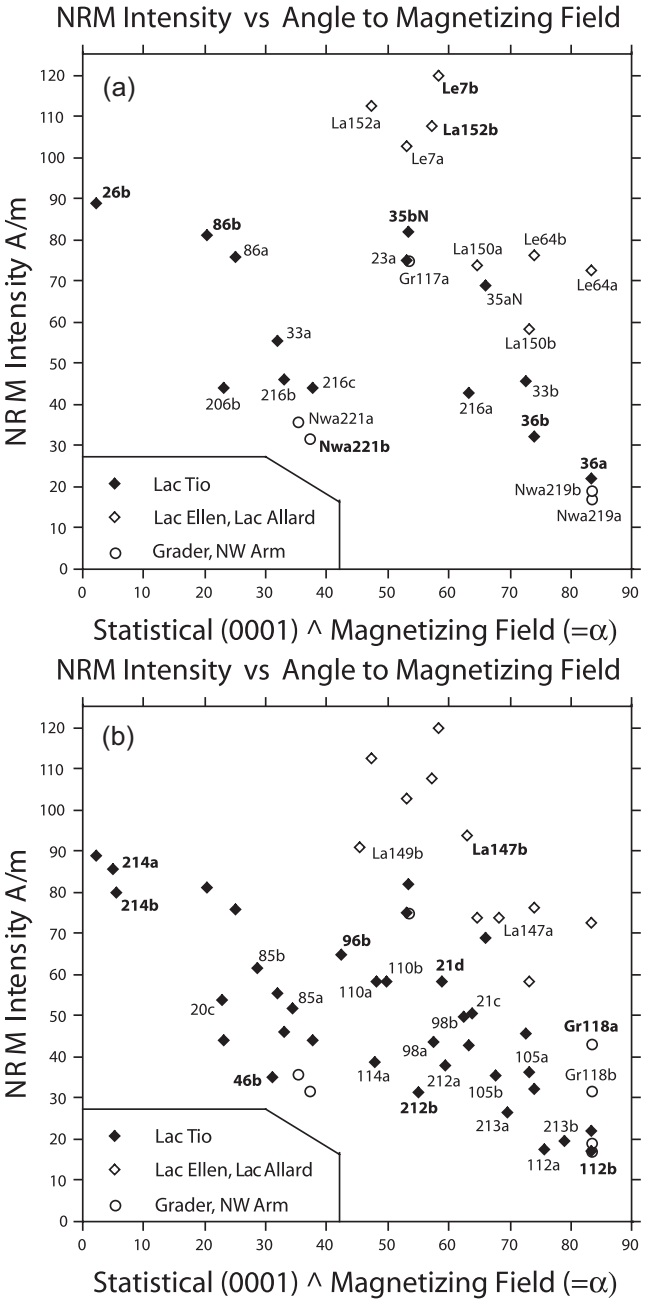

Figure 15. Plot of NRM intensity in A m^{-1} versus α for selected samples with high-quality angular relationships, and low susceptibility for data groups A (a) and A and B (b).

the plot of data points in Fig. 15(a). From Figs 10(b) and 15(a), it can be seen that the intensity of the NRM will be lowest for $\alpha = 0$ and highest for $\alpha = 90^\circ$ consistent with the external force hypothesis (Robinson *et al.* 2004). The trajectory of each sample is flattest near $\alpha = 0^\circ$ and $\alpha = 90^\circ$. The steepness between is a combined function of the intensity potential of the sample and the calculated Fisher distribution K of the crystals (Table E2).

In Fig. 18, sample Nwa221b shows the weakest NRM and a relatively flat slope with an NRM below 5 for $\alpha = 90^\circ$ and only 9 for $\alpha = 0^\circ$. The reversed Lac Tio samples 33a, 36b and 86a have steeper slopes with NRM's 3–25 for $\alpha = 90^\circ$ and 65–95 for $\alpha = 0^\circ$. The Lac Ellen and Lac Allard samples Le7a, Le7b, Le64b, La152a and La152b are in a more magnetic class with yet steeper

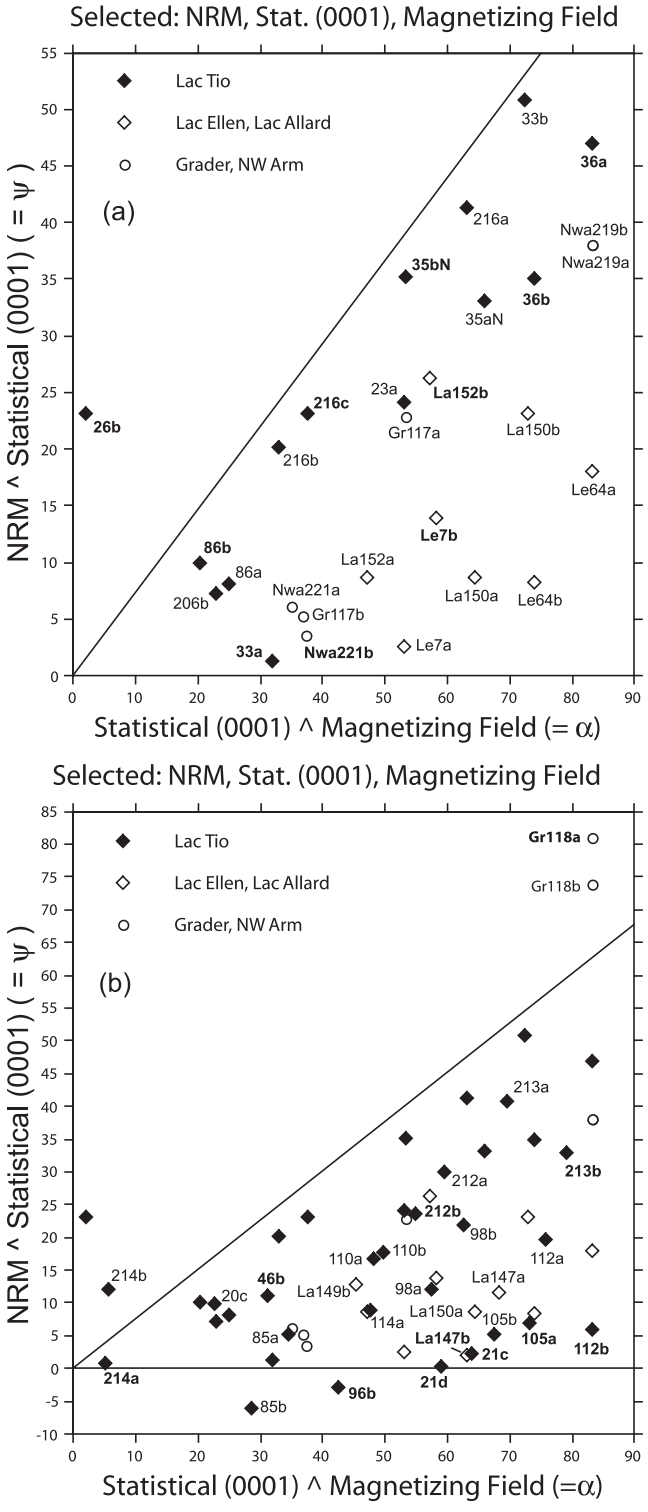

Figure 16. Plot of deviation ψ versus α for selected samples with high-quality angular relationships, and low susceptibility for data groups A (a) and A and B (b).

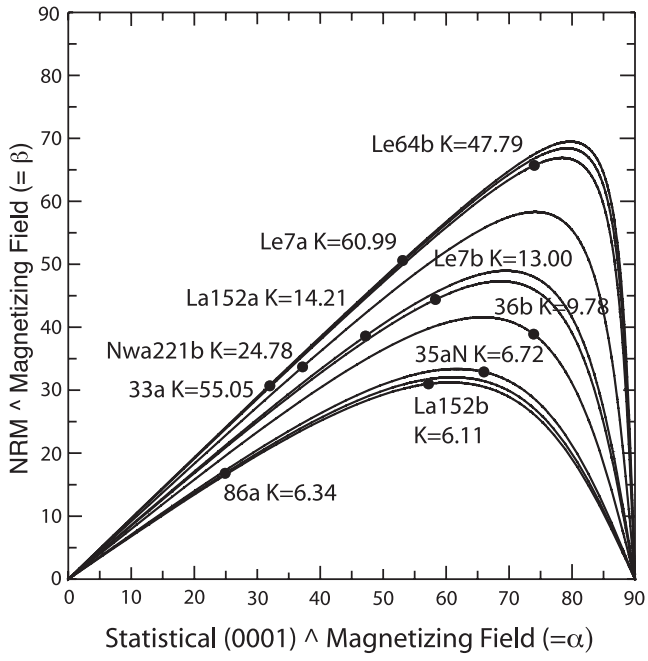

Figure 17. Extrapolations based on Fig. 14 and Appendix C. Plot of the angle β from the NRM to the magnetizing field v versus the angle α of the statistical (0001) basal plane to the magnetizing field v.

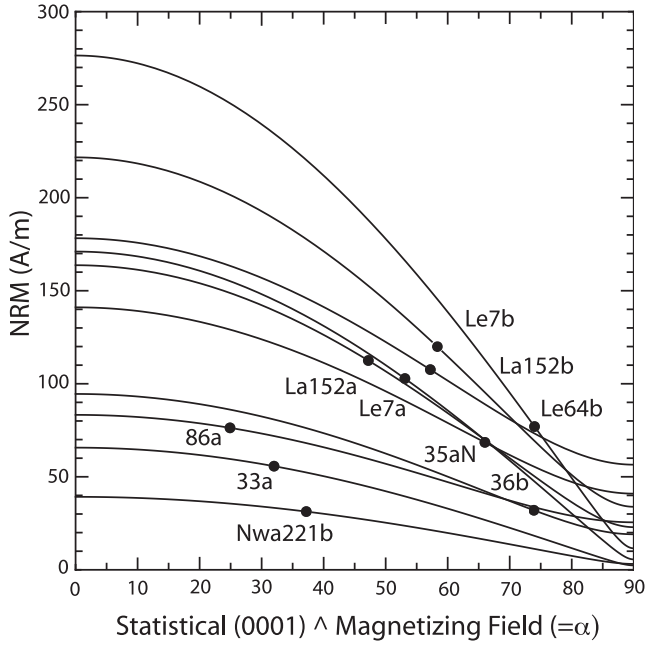

Figure 18. Extrapolations based on Fig. 15 and Appendix C. Plot of NRM intensity in A m^{-1} versus the angle α of the statistical (0001) basal plane to the magnetizing field v.

slopes. These have NRM's 5–57 for $\alpha = 90^\circ$ and 164–277 A m^{-1} for $\alpha = 0^\circ$. The implication of these last data is that if Lac Ellen or Lac Allard samples had formed exsolution lamellae in orientations with (0001) parallel to the Mesoproterozoic magnetizing field, they would have NRM's twice the values measured. This figure quantifies the relationship detected by Hargraves (1959a) between orientation and magnetic intensity, and which he emphasized in support of the lamellar magnetism concept (Robinson *et al.* 2002, 2004).

Fig. 19 shows extrapolations of ψ against α. The graphical arrangement is based on part 3 of Fig. 10(b), and the plot of data points in Fig. 16(a). From Figs 10(b) and 16(a), it can be seen that the value of ψ must be 0° for $\alpha = 0^\circ$ and 90° for $\alpha = 90^\circ$. In between, the trajectory would follow a straight line when the Fisher distribution K approaches zero, and more strongly curved trajectories when the Fisher distribution K is strong (see Table E2), for example, the

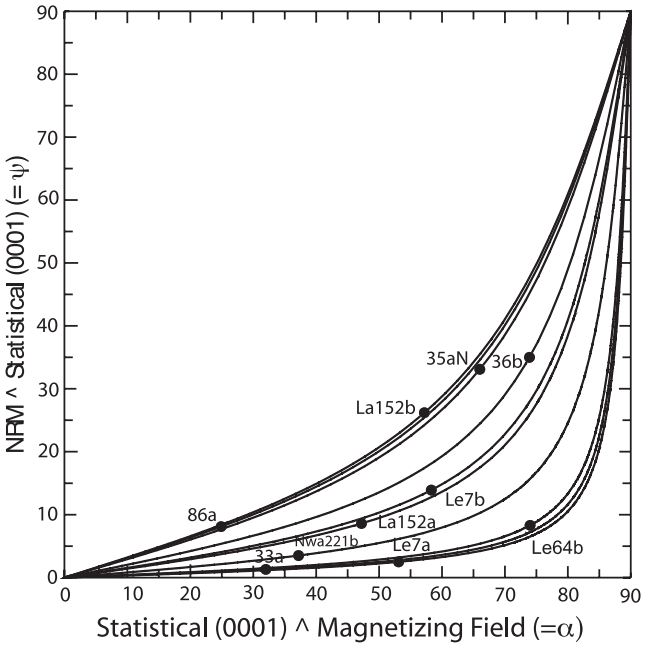

Figure 19. Extrapolations based on Fig. 16 and Appendix C. Plot of deviation ψ of the NRM from the statistical (0001) basal plane versus the angle α of the statistical (0001) basal plane from the magnetizing field v.

calculated trajectories for 33a, Le7a and Le64b. It should be mentioned that Figs 17 and 19 are complementary to each other for the reason that for a circular distribution of platelets, $\psi + \beta = \alpha$.

7 CONCLUSIONS

Magnetic measurements originally made by Hargraves (1959a,b) on a collection of 82 massive hemo-ilmenite samples from the Allard Lake District, Quebec, have been re-assessed, using new experimental and computational approaches, with respect to the origin and intensity of lamellar magnetism, leading to the following insights and conclusions:

(i) The original measurements of orientation of AMS, and declination and inclination of natural remanent magnetism (NRM), indicated a deflection β of the magnetic vector away from the orientation of the Mesoproterozoic magnetizing field **v**, caused by LPO, in particular the statistical (0001) basal plane, to which the NRM is confined in single crystals.

(ii) A second deflection ψ that is the angle the NRM makes with the statistical (0001) basal plane of the crystal assemblage was determined.

(iii) Combining ψ with α, the angle of the statistical (0001) basal plane with the magnetizing field **v**, it is possible to calculate a function y that is equivalent to K, the Fisher distribution of crystal platelets.

(iv) By using k_3/k_1 from the AMS measurements, it is possible to calculate k_3^0/k_1^0, the single crystal anisotropy of individual platelets. This showed that typical crystals of hemo-ilmenite have a relatively weak AMS so that even samples with a very narrow Fisher distribution K of plates nevertheless can show a correspondingly weak AMS.

(v) Measurements of (0001) basal plane distributions using EBSD were made in two samples, 36b and Le7b. Measurements of the AMS and NRM of a single extracted hemo-ilmenite crystal from 36b confirm the above conclusion.

(vi) Based on a conceptual model, and on y and K values calculated from ψ and α of selected samples, we calculate values of β, NRM intensity and ψ for any value of α. For the Lac Tio group of samples, NRM intensity ranges from 3 to 25 A m^{-1} for $\alpha = 90^\circ$ to 65–95 A m^{-1} for $\alpha = 0^\circ$. For the Lac Ellen–Lac Allard group of samples, NRM intensity ranges from 5 to 57 A m^{-1} for $\alpha = 90^\circ$ to 164–277 A m^{-1} for $\alpha = 0^\circ$. These results provide striking examples of the influence of the external force of the magnetic field with respect to the orientation of the crystal LPO, at the time magnetization was acquired, in determining the intensity of NRM.

ACKNOWLEDGMENTS

Ann M. Hirt, ETH, Zürich, kindly provided the NRM and AMS measurements of the extracted single hemo-ilmenite crystal from sample 36b as part of another project, for which we previously obtained the crystallographic orientations by EBSD (Fig. 2 A). Hubert Schulze, BGI, Bayreuth, used the information in Fig. 2(a) to prepare a polished surface precisely oriented normal to the (0001) basal plane and containing the NRM that is shown in Fig. 2(b). Valeriy Shcherbakov, Geophysical Observatory of the Russian Academy of Science, Borok, provided his calculation of the magnetic susceptibility of $FeTiO_3$. This permitted us to calculate a value for magnetite-free Allard Lake hemo-ilmenite used in Section 3.5. Tullis Onstott, Princeton University, searched unsuccessfully there for additional orientation information on Hargraves samples from Allard Lake. This research was supported by grant 189721 from the Research Council of Norway (Nanomat Program) in the EU Matera Program. The late stages in manuscript preparation took place while Robinson and McEnroe were resident at BGI, Bayreuth, where McEnroe held a Marie Curie Fellowship under the sponsorship of Prof. Falko Langenhorst. The manuscript benefited from constructive suggestions of Fatima Martin-Hernandez and an anonymous reviewer. To each of these persons and institutions, we extend our grateful acknowledgment.

REFERENCES

Bourret, W., 1959. Aeromagnetic survey of the Allard Lake district, Quebec, *Econ. Geol.,* **44,** 732–740.

Carmichael, C.M., 1959. Remanent magnetization of the Allard Lake ilmenites, *Nature,* **183,** 1239–1241.

Fabian, K., McEnroe, S.A., Robinson, P. & Shcherbakov, V., 2008. Exchange bias identifies lamellar magnetism as the origin of the natural remanent magnetization in titanohematite with ilmenite exsolution from Modum, Norway, *Earth planet. Sci. Lett.,* **268,** 339–353.

Fabian, K., Robinson, P., McEnroe, S.A., Heidelbach, F. & Hirt, A.M., 2011. Experimental study of the magnetic signature of basal-plane anisotropy in hematite, in *The Earth's Magnetic Interior,* vol. 1 of IAGA Special Sopron Book Series, pp. 311–320, Springer-Verlag, Berlin, Heidelberg, New York.

Flinn, D., 1962. On folding during three-dimensional progressive deformation, *Quart. J. geol. Soc. London,* **118,** 385–433.

Guerrero-Suárez, S. & Martin-Hernandez, F., 2012. Magnetic anisotropy of hematite natural crystals: increasing low-field strength experiments, *Int. J. Earth Sci.,* **101,** 625–636.

Hammond, P., 1952. Allard lake ilmenite deposits, *Econ Geol.,* **47,** 636–649.

Hargraves, R.B., 1959a. Magnetic anisotropy and remanent magnetization in hemo-ilmenite from ore deposits of Allard Lake, Quebec, *J. geophys. Res.,* **64,** 1565–1573.

Hargraves, R.B., 1959b. Petrology of the Allard lake anorthosite suite, and paleomagnetism of the ilmenite deposits, *PhD thesis,* Princeton University.

Hargraves, R.B. & Burt, D.M., 1967. Paleomagnetism of the Allard Lake anorthosite suite, *Can. J. Earth Sci.,* **4,** 357–369.

Harrison, R.J. & Becker, U., 2001. Magnetic ordering in solid solutions, in *Solid Solutions in Silicate and Oxide Systems,* Vol. 3, pp. 349–383, European Mineralogy Union Notes in Mineralogy. European Mineralogical Union.

Hrouda, F., Siemes, H. & Herres, N. C. H.-M.1985. The relationship between the magnetic anisotropy and the c-axis fabric in a massive hematite ore, *J. Geophys.,* **56,** 174–182.

Mainprice, D., 1990. A Fortran program to calculate seismic anisotropy from the lattice preferred orientation of minerals, *Comput. Geosci.,* **16,** 385–393.

Martin-Hernandez, F. & Guerrero-Suárez, S., 2012. Magnetic anisotropy of hematite natural crystals: high field experiments, *Int. J. Earth Sci.,* **101,** 637–647.

McCammon, C., McEnroe, S.A., Robinson, P., Fabian, K. & Burton, B.P., 2009. Mössbauer spectroscopy used to quantify natural lamellar remanent magnetization in single-grains of ilmeno-hematite, *Earth planet. Sci. Lett.,* **288,** 268–278.

McEnroe, S.A. & Brown, L.L., 2000. A closer look at remanence dominated anomalies: rock-magnetic properties and magnetic mineralogy of the Russell Belt microcline-sillmanite gneisses Northwest Adirondacks mountains, New York, *J. geophys. Res.,* **105,** 16 437–16 456.

McEnroe, S.A., Harrison, R., Robinson, P., Golla, U. & Jercinovic, M.J., 2001. The effect of fine-scale microstructures in titanohematite on the acquisition and stability of NRM in granulite facies metamorphic rocks from southwest Sweden: implications for crustal magnetism, *J. geophys. Res.,* **106,** 30 523–30 546.

McEnroe, S.A., Harrison, R.J., Robinson, P. & Langenhorst, F., 2002. Nanoscale haematite-ilmenite lamellae in massive ilmenite rock: an example of 'lamellar magnetism' with implications for planetary magnetic anomalies, *Geophys. J. Int.,* **151,** 890–912.

McEnroe, S.A., Carter-Stieglitz, B., Harrison, R.J., Robinson, P., Fabian, K. & McCammon, C., 2007a. Magnetic exchange bias of more than 1 Tesla in a natural mineral intergrowth, *Nature Nanomater.,* **2,** 631–634.

McEnroe, S.A., Robinson, P., Langenhorst, F., Frandsen, C., Terry, M. & Ballaran, T.B., 2007b. Mineral chemistry, phase relations and magnetic properties of hemo-ilmenite ores with micron- to nanometer-scale exsolution lamellae from Allard Lake, Quebec: implications for planetary magnetization, *J. geophys. Res.,* **112,** doi:10.1029/2007JB004973.

Robinson, P., Harrison, R.J., McEnroe, S.A. & Hargraves, R.B., 2002. Lamellar magnetism in the haematite-ilmenite series as an explanation for strong remanent magnetization, *Nature,* **418,** 517–520.

Robinson, P., Harrison, R.J., McEnroe, S.A. & Hargraves, R.B., 2004. Nature and origin of lamellar magnetism in the hematite-ilmenite series, *Am. Mineral.,* **89,** 725–747.

Robinson, P., Harrison, R.J. & McEnroe, S.A., 2006a. Fe^{2+}/Fe^{3+} charge ordering in contact layers of lamellar magnetism: bond valence arguments, *Am. Mineral.,* **91,** 67–72.

Robinson, P., Heidelbach, F., Hirt, A.M., McEnroe, S.A. & Brown, L.L., 2006b. Crystallographic-magnetic correlations in single-crystal haemo-ilmenite: new evidence for lamellar magnetism, *Geophys. J. Int.,* **165,** 17–31.

Siemes, H., Schaeben, H., Rosiere, C.A. & Quade, H., 2000. Crystallographic and magnetic preferred orientation in banded iron ores, *J. Struct. Geol.,* **22,** 1747–1759.

APPENDIX A: CORRECTION OF NRM DATA

Some of Hargraves' Allard Lake samples, first studied in 1959, were re-examined by Hargraves in the 1980's and others by McEnroe in 2001–2003. Re-examination indicated that the NRM values reported in cgs units in the 1959 paper and thesis were too small by a crude factor of 10. However, later notes by Hargraves indicated that the earlier results can be converted to SI units by multiplying by 4π. Remeasured values and examples of corrections are given in Table A1.

Table A1. Corrections of NRM intensites for Allard lake samples.

Sample	NRM 1959 (cgs)	NRM 1959[3] (SI)	Newer NRM (SI)
20a	4.59[1]	57.7	53[H]
20c	4.28	53.8	43[M]
20d	4.9	61.6	
23a	5.99	75.3	
23b	6.22[2]	78.1	77[M]
23c	6.45	81.1	93.4[H]
26b	7.07	88.8	91.2[H]
36b	2.1	26.4	32[M]
46b	2.8	35.2	(73[M])[4]
112a	1.35	17.0	11.6[H]
114b	3.5	44.0	34[M]
Le7a	8.18	102.8	95[H]
Le7b	9.35	117.5	120[M]

Notes:
[1]Mean value from companion samples AL20c and Al20d.
[2]Mean value from companion samples AL23a and AL23c.
[3] Hargraves (1959a,b) reported cgs units $\times 4\pi$.
[H]Hargraves's (1980), personal communication 2001–2002.
[M]McEnroe *et al.* (2001–2002).
[4]Values show extreme difference from earlier measurement, suggesting an error.

APPENDIX B: CONSEQUENCES OF BASAL PLANE ANISOTROPY FOR DETERMINING THE MAGNETIZING FIELD

A crystallographically controlled positioning of the NRM within the basal plane of single crystals can provide situations where the GC containing the *c*-axis (and k_3-axis of the AMS) and the NRM of a specimen does not pass through the vector of the magnetizing field **v**. To the extent that this is true, it would violate the prescriptions used by Hargraves (1959a) to locate the magnetizing field.

For purpose of discussions, consider a hemo-ilmenite crystal similar to the one in Fig. 2, where the NRM seems to be constrained to one of the crystallographic *a*-axes and also to the k_2-axis of the AMS. A corresponding constraint appears to be present in a hematite single crystal studied in detail by Fabian *et al.* (2011). Related results are reported by Guerrero-Suárez & Martin-Hernandez (2012); Martin-Hernandez & Guerrero-Suárez (2012). However, in hematite, the spin-canted NRM vector would bisect the angle between two *a*-axes. Robinson *et al.* (2006b) speculate that the NRM orientation of lamellar magnetism could be a compromise between uncompensated spins at lamellar interfaces parallel to *a*-axes and the spin-canted component of hematite bisecting the angle between those axes.

First consider a crystal positioned so that a crystallographically constrained NRM lies on GC containing the k_3 AMS axis (crystallographic *c*-axis) and the magnetizing field vector **v** as in Fig. B1(a). This crystal fulfils the Hargraves prescription in spite of the constraint. Now consider where the same crystal is oriented so that the NRM is oriented 30° away from the previous position as in Fig. B1(b). Here, the GC containing the NRM and k_3-axis will not pass through magnetizing field vector **v**, except in the special case where k_3 is parallel to **v**. The angle between GC and **v** will increase

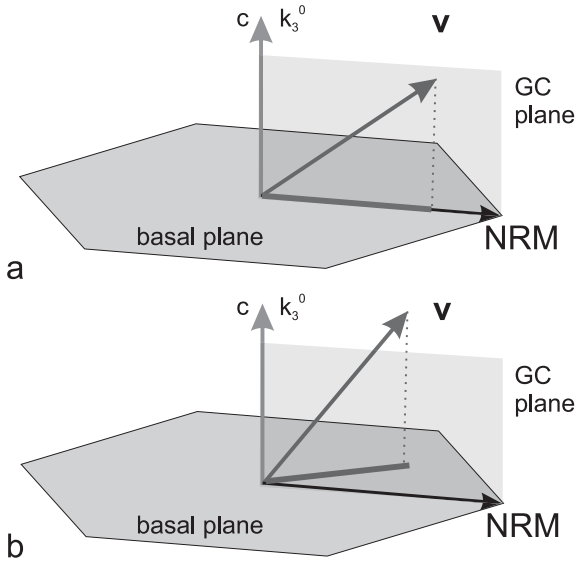

Figure B1. Effect of crystallographic constraint on the position of the NRM within the basal plane of a single crystal of hemo-ilmenite. (a) The NRM in the basal plane is positioned with respect to the magnetizing vector **v** such that the GC containing the NRM and the *c*-axis (k_3^0 of the AMS) passes through the magnetizing vector. This crystal fulfills the Hargraves criteria. (b) The NRM in the basal plane is positioned with respect to the magnetizing vector such that GC containing the NRM and k_3^0 does not pass through the magnetizing vector, thus failing the Hargraves criteria. Failure can reach a maximum of 30° when k_3^0 is nearly parallel to the magnetizing field (see text).

as the angle between **v** and k_3 increases until they are perpendicular, where the angle of GC to **v** reaches a maximum at 30°. This would be a serious problem if finding the orientation of paleomagnetic **v** depended on a single crystal; however, specimens are composed of hundreds of crystals with varying orientations and this mitigates the problem.

As an initial approximation, consider an assemblage of crystals with a strong orientation of *c*-axes, but random orientation of *a*-axes. Quite obviously this would eliminate the problems related to the single crystals, providing a circular anisotropy that completely fulfills the Hargraves criteria. However, the single-crystal difficulties could be retained if the deformation mechanism, about which little is known, also created a preferred orientation of *a*-axes, the NRM and k_2 in the basal plane. Examination of the two equal area diagrams in Fig. D1, showing the distributions of *a*-axes in samples Le7b and 36b, suggests that this may be true at least in these two samples, though a degree of scatter along the basal plane provides a tendency toward circular distribution. Consider two examples with tight *a*-axis distributions. In example A, despite the anisotropy, the NRM lies exactly on the GC containing k_3 and the magnetizing field vector **v**. The Hargraves criteria are still fulfilled. In example B, the NRM lies about 30° on either side of the position in example A so that the GC containing k_3 and an NRM would have a maximal angle from **v**, and poor adherence to the Hargraves criteria among the single crystals. However, if the alignment is somewhat imperfect in the assemblage, with some crystals 28°–29° one way and others 28°–29° the other from the average 30° position, each group will provide fairly large deflections, but in opposite directions. Here, opposite deflections of the GC planes will be averaged out, resulting in little or no overall deflection, as prescribed by Hargraves.

Above we described one way to obtain a triaxial anisotropy ellipsoid in an assemblage of hemo-ilmenite platelets. Another likely process is folding of the foliation (Siemes *et al.* 2000). In such an example, the k_1-axis would lie parallel to the fold axis, the k_2-axis would be a statistical average of multiple variably oriented basal planes, and the k_3-axis will be a similar average of variably oriented low-susceptibility directions normal to basal planes. In such an arrangement, k_1 could be slightly less than that of a relevant crystal, k_2 would be lower and k_3 would be higher.

To test this, we sorted the 80 specimens into three groups: I–8 (10 per cent) where $k_1 = k_2$ indicating a perfectly circular ellipsoid totally fulfilling the Hargraves criteria; II–53 (66 per cent) with k_1/k_2 in the range of 1.01–1.09 indicating ellipsoids that are not far from circular; and III–19 (23.8 per cent) with $k_1/k_2 > 1.09$ indicating significantly triaxial ellipsoids. We hoped to evaluate results from some of the most triaxial examples, but that was impossible because Hargraves never recorded inclinations and declinations of k_1 and k_2 AMS axes, only k_3. We did perform paleomagnetic tests, using the above three groups, also the same groups narrowed to the A and B quality classes described elsewhere. We reasoned that, if specimens, with significant basal plane anisotropy in their statistical AMS ellipsoids, do, in fact, seriously bias the determined magnetizing field direction **v**, then that would show up.

Geometric results on hemo-ilmenites were as follows: 80 as plotted in Figs 12(a) and (b)—74.0°, 86.8°; 49 Lac Tio—64.1°, 79.8°; 8 Group I $k_1/k_2 = 1.00$—111.8°, 83.6°; 6 Group I A+B $k_1/k_2 = 1.00$—79.8°, 80.0°; 53 Group II $k_1/k_2 = 1.01$–1.09-72.8°, 85.5°; 36 Group II A+B $k_1/k_2 = 1.01$–1.09—43.0°, 80.4°; 19 Group III $k_1/k_2 \geq 1.09$—256.0°, 82.9°; 11 Group III A+B $k_1/k_2 \geq 1.09$—43.0°, 80.4°; 26 Class A—34.9°, 81.2°. Although the declinations seem variable, with such high inclinations, angular differences are very small, and only 256.0°, 82.9° is more than 10° outside the group. We also list four conventional remanent vectors from Hargraves & Burt (1967): Lac Tio anorthosite—64.6°, 80.1°; Lac Allard -MacRae norite (6.5 km from Lac Tio) - 146.9°, 83.8°; Grader norite (3 km from Lac Tio)—115.7°, 77.2°; Puyjalon anorthosite, norite (5 km from Lac Tio)—131°, 70°. The last three may have a different cooling history.

The above discussion and geometric results lead to the following conclusion. A triaxial AMS ellipsoid produced by single-crystal basal-plane anisotropy, or by folding of basal plane foliation in an assemblage of crystals can, in theory, influence the orientations of GC planes used to locate the paleomagnetic vector **v**, but the effect is small and generally averaged out. In comparison to normal paleomagnetic practice, the Hargraves approach is vindicated.

APPENDIX C: NRM AND AMS OF A FISHER-DISTRIBUTED ASSEMBLY OF PLATELETS

Here, we present theoretical considerations aiming to develop a quantitative understanding of the connections between 1) the AMS of the individual crystals, $\sigma^0 = k_3^0/k_1^0$, 2) the AMS of the natural crystal assemblages, $\sigma = k_3/k_1$, 3) the NRM deflection angle β with respect to the external field and 4) the NRM deflection angle ψ from the (0001) basal plane.

The geometric configuration and terminology is shown in Fig. 9. To simplify the model, it is assumed that the *c*-axes of the individual crystals are randomly scattered around a mean *c*-axis of the assemblage, and that this scatter follows a rotationally symmetric Fisher distribution.

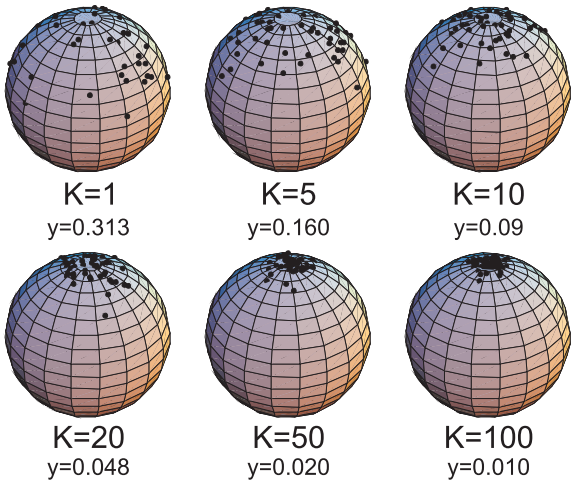

Figure C1. The parameter K of the Fisher distribution determines the scatter of the individual c-axes (black dots) with respect to the statistical c-axis, which corresponds to the z-axis. The panels also report the equivalent y parameter.

C1 Fisher distribution of *c*-axes

The rotationally symmetric Fisher-distribution of the individual c-axes around the axis $\theta = 0$ is defined by

$$f(\theta) = \frac{K\ \cosh(K\ \cos\theta)}{2\pi\ \sinh K}, \tag{C1}$$

where $K \geq 0$ is a concentration parameter and $f(\theta)$ denotes the probability to find an individual crystal of the assemblage with tilt angle θ away from the mean c-axis. Each individual axis is represented by its pole (θ, ϕ) in the upper hemisphere, $\theta \leq \pi/2$. Due to rotational symmetry, the distribution f does not depend on ϕ. Equi-distribution occurs for $K = 0$, while for $K \to \infty$, the distribution approaches a point distribution at $\theta = 0$. The normalization is chosen such that the spherical integral is unity:

$$\int_{\theta=0}^{\pi/2}\int_{\phi=0}^{2\pi} f(\theta)\ \sin\theta\ \mathrm{d}\phi\ \mathrm{d}\theta = 1. \tag{C2}$$

To describe an anisotropic assemblage of planar crystals, it is assumed that their c-axes are distributed in this way for some K. The fraction of c-axes in the spherical cap of angle θ_0 around $\theta = 0$ is then given by

$$\int_{\theta=0}^{\theta_0}\int_{\phi=0}^{2\pi} f(\theta)\ \sin\theta\ \mathrm{d}\phi\ \mathrm{d}\theta = 1 - \frac{\sinh(K\ \cos\theta_0)}{\sinh K}. \tag{C3}$$

Fig. C1 shows 50 randomly Fisher-distributed points on a sphere (upper hemisphere) for different values of K. Based on the assumptions about the AMS and the NRM acquisition of the individual crystals, it is possible to calculate these two quantities for any crystal assemblage with a chosen distribution of c-axes, described by the scatter parameter K.

C2 Natural remanent magnetization

Assuming NRM acquisition of an individual platelet to be linear with field strength, and to occur only perpendicular to its c-axis, the remanence $\mathbf{m}^0$ acquired by a platelet with individual c-axis parallel

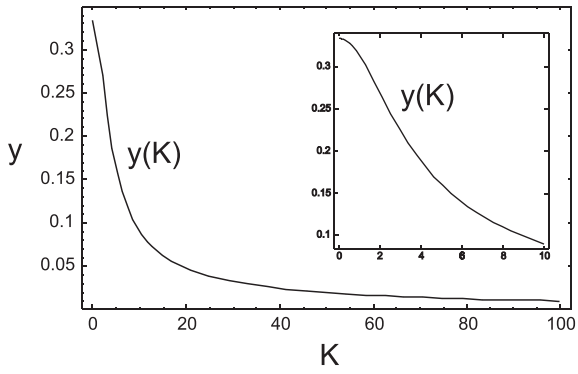

Figure C2. The scatter parameter K of the Fisher distribution and the parameter $y(K) = (K\ \coth K - 1)/K^2$ are in one-to-one correspondence. $y(K)$ decreases from $y(0) = 1/3$ to zero for increasing K.

to the unit vector $\mathbf{n}^0$, and maximal moment $m^0_{\max}$, in an external field $H\,\mathbf{v}$ is

$$\mathbf{m}^0(\mathbf{n}^0) = m^0_{\max}\ H\ \left(\mathbf{v} - (\mathbf{v}\cdot\mathbf{n}^0)\,\mathbf{n}^0\right). \tag{C4}$$

For the rotational symmetric distribution (C1), the NRM lies in the plane spanned by field and statistical c-axis. Without loss of generality, this plane is assumed to be the xz-plane. Therefore, when the angle between field and statistical (0001)-plane is α (Fig. 9), and

$$\mathbf{n}^0 = \begin{pmatrix}\sin\theta\cos\phi\\ \sin\theta\sin\phi\\ \cos\theta\end{pmatrix},\ \mathbf{v} = h\begin{pmatrix}\cos\alpha\\ 0\\ \sin\alpha\end{pmatrix}, \tag{C5}$$

one obtains for the individual remanence

$$\mathbf{m}^0(\theta,\phi) = m^0_{\max}\ H\ \left(\mathbf{v} - (\cos\alpha\sin\theta\cos\phi + \cos\theta\sin\alpha)\,\mathbf{n}^0\right). \tag{C6}$$

Integrating this remanence over the Fisher distribution from the previous section yields the NRM of the assemblage

$$NRM(\mathbf{v}) = m^0_{\max}\ H\begin{pmatrix}(1 - y(K))\ \cos\alpha\\ 0\\ 2\,y(K)\ \sin\alpha\end{pmatrix}, \tag{C7}$$

where

$$y(K) = \frac{K\ \coth(K) - 1}{K^2} \tag{C8}$$

decreases from $y(0) = 1/3$ to 0 for increasing K as shown in Fig. C2.

This result quantifies how NRM strength, and angular deviation between $NRM(\mathbf{v})$ and $\mathbf{v}$ depend upon the distribution width K. This relation is simplest for the ratio between the NRM components parallel and perpendicular to the statistical c-axis. Using the angle ψ from Fig. 9, one obtains

$$\frac{NRM_\parallel}{NRM_\perp} = \tan\psi = \frac{2y}{1-y}\ \tan\alpha, \tag{C9}$$

which is solved for y to yield

$$y = \frac{\tan\psi}{2\ \tan\alpha + \tan\psi}. \tag{C10}$$

By numerically solving (C8) for K, one obtains an estimate of the Fisher-distribution width K from the measured angles ψ and α. For the assumed case, where the NRM vector lies in the plane spanned by field and statistical c-axis (see Fig. 9 for geometry). Fig. C3 shows the theoretical dependence of the measured angle $\beta = \alpha - \psi$ on α for different values of K.

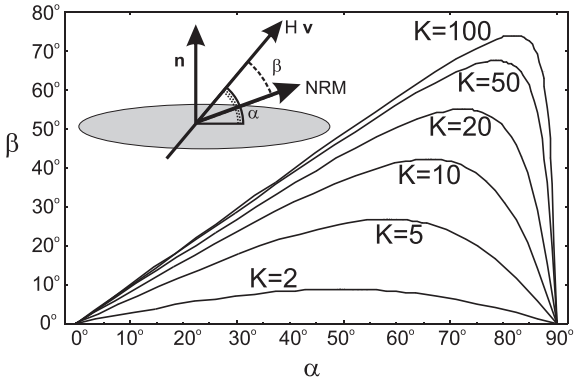

Figure C3. Model prediction for the dependence of the angle β between the NRM vector and field direction upon the angle α between field direction and statistical basal plane. When the scatter is large ($K = 2$), β stays small, indicating that the NRM can align well with the field. When the distribution becomes narrow ($K = 100$), the angle β at first increases linearly with α, but then drops sharply to 0° (see Fig. 7) when the area of *c*-axis scatter contains sufficiently many individual axes with more than 90° deviation from the field direction. Then, the residual NRM can align well with the field by inverse magnetization of these directions.

C3 Anisotropy of magnetic susceptibility

For an individual crystal with *c*-axis parallel to the unit vector $\mathbf{n}^0$, the susceptibility has the minimal value k_3^0 parallel to the *c*-axis, and the maximum value k_1^0 perpendicular to the *c*-axis. Its susceptibility along the unit field vector $\mathbf{v}$ accordingly is

$$k(\mathbf{v}) = k_1^0 - \Delta k^0 \, (\mathbf{v} \cdot \mathbf{n}^0)^2, \tag{C11}$$

where $\Delta k^0 = k_1^0 - k_3^0 \geq 0$. Substituting from (C5), and integrating (C11) over the Fisher distribution of the individual $\mathbf{n}^0$ yields the assemblage susceptibility as a function of α

$$k(\alpha) = k_1^0 - y(K)\, \Delta k^0 - (1 - 3\, y(K))\, \Delta k^0 \, \sin^2 \alpha. \tag{C12}$$

This expression describes an anisotropy ellipsoid with minimal susceptibility k_3 along the assemblage *c*-axis $\theta = 0$, and maximal susceptibility k_1 in the statistical (0001) basal plane. For the corresponding values

$$k_1 = k_1^0 - y(K)\, \Delta k^0, \, k_3 = k_3^0 + 2\, y(K)\, \Delta k^0, \tag{C13}$$

one has the intuitively obvious relations $k_1 \leq k_1^0$ and $k_3 \geq k_3^0$.

C4 Analysis of the result

Eqs (C7) and (C13) show that both NRM and susceptibility depend on K only through the function $y(K)$. It is easier to directly use y to describe the concentration of the Fisher distribution. In this case, $y = 0$ corresponds to a point distribution at $\theta = 0$, while $y = 1/3$ represents equi-distribution of the axes. By introducing the individual AMS ratio $\sigma^0 = k_3^0/k_1^0$ and the corresponding assemblage ratio $\sigma = k_3/k_1$, (C13) can be written as

$$\sigma = \frac{2\, y + \sigma^0 \, (1 - 2\, y)}{1 - y + \sigma^0 \, y}. \tag{C14}$$

Assuming that y is known, for example, from (C10), this allows determination of σ^0 from σ and y by

$$\sigma^0 = \frac{\sigma - y\,(2 + \sigma)}{1 - y\,(2 + \sigma)}. \tag{C15}$$

Substituting (C10) into (C15) yields a relationship connecting AMS ratios and deflection of NRM. This equation links the NRM measurements, which allows estimation of y, to the independent AMS data to predict the intrinsic AMS of the individual crystals involved. An additional complication occurs for samples containing a certain fraction of multi-domain magnetite, which contributes little to the NRM, but substantially increases magnetic susceptibility. In rare cases where the MD magnetite replaces the hematite lamellae, it has the same morphology and texture, and accordingly, may assume a shape anisotropy which has the same orientation as the original hematite anisotropy. This can be described by adding two constants, $k_{\mathrm{mt},\,1}$ and $k_{\mathrm{mt},\,3}$, to the right-hand sides of both equations in (C13), which finally yields

$$\sigma = \frac{2\, y + \xi_3 + \sigma^0 \, (1 - 2\, y)}{1 + \xi_1 - y + \sigma^0 \, y}, \tag{C16}$$

where $\xi_1 = k_{\mathrm{mt},1}/k_1^0$ and $\xi_3 = k_{\mathrm{mt},3}/k_1^0$ are the relative susceptibilities of the magnetite fraction. If the magnetite occurs as independent isotropic mineral fraction, one simply has $\xi_1 = \xi_3$ and it contributes little to the AMS.

APPENDIX D: FISHER DISTRIBUTION OF *c*-AXES COMPARED TO AMS

In Appendix C, we showed that there is a correlation between the Fisher distribution K of *c*-crystallographic axes in a crystal assemblage and the magnetic anisotropy of individual crystals. The deviation angle ψ is a function of K in Fig. C3, and it is also a function of k_2/k_3 (or k_1/k_3 for circular distributions) as in Fig. 11. An important outcome of these comparisons is to show that the ratio k_1^0/k_3^0 of individual crystals is not large. A consequence of this is that a low anisotropy of the AMS can reflect a very strong Fisher distribution of *c*-axes. We have made a test of this by measuring the real distribution of *c*-axis orientations in samples Le7b and 36b by EBSD, and then calculating the AMS from these distributions using the single-crystal AMS data provided by single crystal #19 extracted from sample 36b.

For measurements of sample Le7b, in which a study was made of both polished surfaces of a 2.5 cm core slice, the number of *c*-axis orientations is over 22 000. For sample 36b, we retained the more limited number of 40 *c*-axis orientations to go with the excellent data from the single crystal. We did not obtain an individual single crystal from the Le7b assemblage and have used the 36b single-crystal data as a proxy to calculate a theoretical AMS from this assemblage. The fact that the calculated AMS based on the EBSD data (Table E1) is not very far from the AMS measured on sample Le7b suggests that the anisotropy of Le7b crystals is not greatly different from 36b crystals, even though they contain a stronger NRM. We are still not sure why the same construction using the more limited EBSD data from sample 36b indicates a higher anisotropy than was actually measured.

Fig. D1 shows the results related to the EBSD study with contoured lower hemisphere equal area diagrams based on the 22 112 and 40 individual measurements of *c*-crystallographic axes from Le7B (Fig. D1 a) and 36b (Fig. D1 b), respectively, and corresponding *a*-axes. The maximum contour densities for *c*-axes are 25 and 22 times as dense as would be true for random distributions, indicating very strong but slightly differing LPOs of (0001) basal planes. Part C is a contoured lower hemisphere pole figure showing the intensity of magnetic susceptibility in all directions for crystal #19 from sample 36b. Parts D and E show how the single-crystal data of part C was used in conjunction with the EBSD data in a program of Mainprice (1990) to calculate a contoured diagram for the

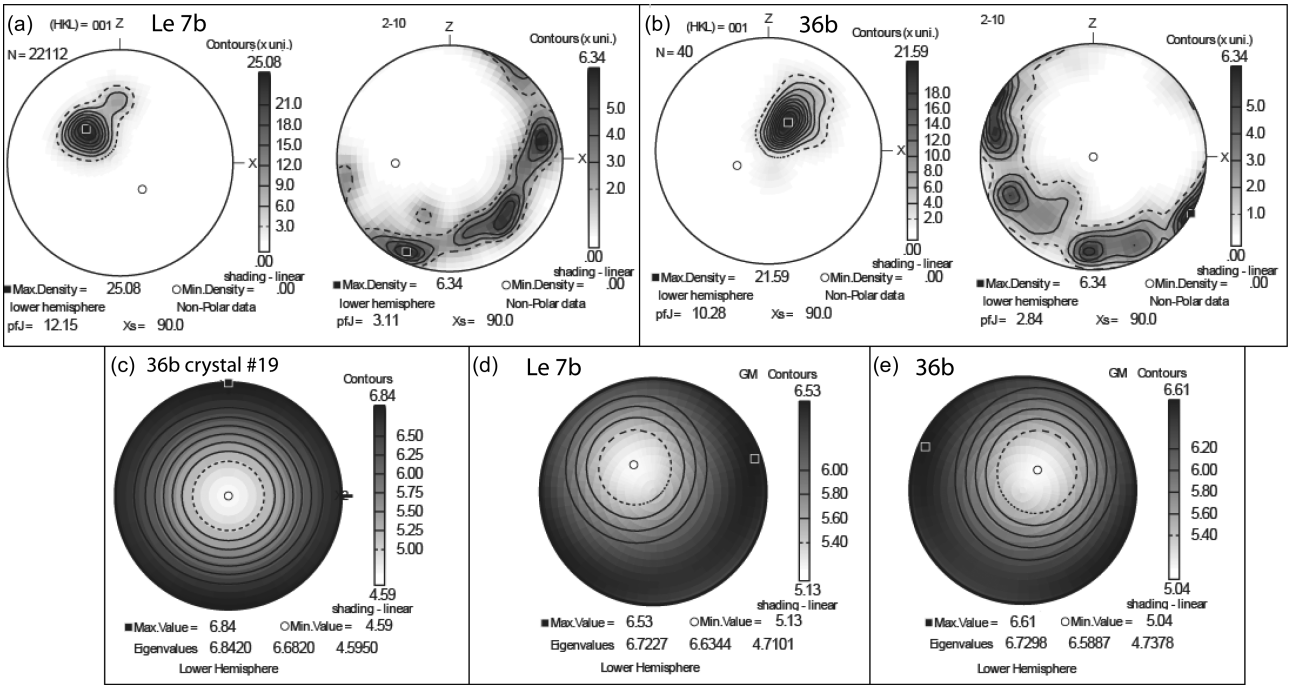

Figure D1. Results related to the EBSD study of samples 36b and LE7b. (a) and (b) Contoured lower hemisphere equal area diagrams for Le7b and 36b based on 22 112 and 40 individual measurements of *c*-crystallographic axes and corresponding a axes. (c) Contoured lower hemisphere pole figure showing the intensity of magnetic susceptibility in all directions for crystal #19 from sample 36b. (d) and (e) Single-crystal data of (c) used in conjunction with the EBSD results creating contoured diagrams for Le7b and 36b crystal assemblages, respectively, and eigenvectors showing the predicted susceptibility in three directions for each.

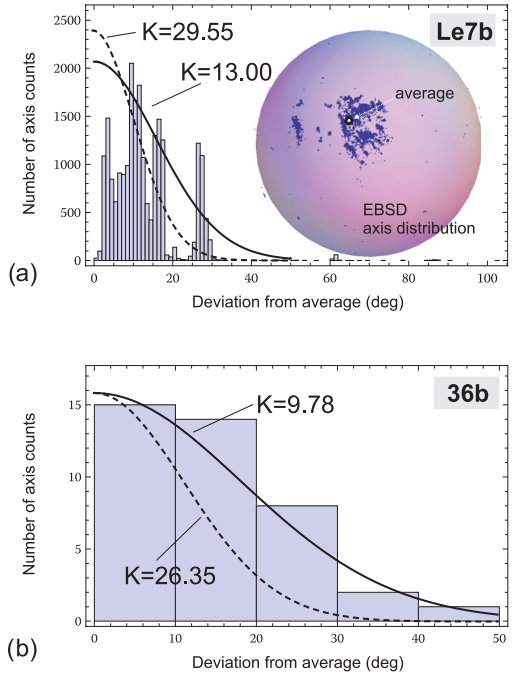

Figure D2. Comparison of distributions of ilmenite *c*-axes determined by EBSD, with distributions determined from values of *K* calculated magnetically (solid lines), and with distributions from values of *K* calculated using combined results (dashed lines) in Fig. D1 and Table E1. (a) Results for sample Le 7b showing both a hemispheric projection of 22 112 points, and a rotationally symmetric histogram about the average orientation. (b) Results for sample 36b showing a rotationally symmetric histogram of 40 points about the average orientation.

Le7b and 36b crystal assemblages, and also eigenvectors showing the predicted susceptibility in three directions. Table E1 contains the AMS input data for crystal #19 with its AMS ratios, the measured AMS ratios for samples 36b and Le7b, and the derived susceptibility data and AMS ratios based on the calculation procedure outlined by Mainprice (1990).

A direct comparison of EBSD results for the distribution of hemo-ilmenite crystallographic *c*-axes in samples Le7b and 36b with estimations of *K* for each by two methods is shown in Fig. D2. For the magnetic measurements, *K* is obtained by solving eq. (C10) for *y* and then *K* is solved numerically (Table E2). From the EBSD measurements, *K* is obtained by solving eq. (C14) or (C15) for *y*, based on the results given in Fig. D1 and Table E1, then again solving for *K* numerically (Table E3). Table E1 results reflect the fact that the Mainprice (1990) program considers axis distributions as elliptically distributed on a hemispheric surface, whereas the histograms in Fig. D2 and the direct magnetic calculations consider a rotationally symmetric distribution about the average. For sample Le7b, 22 112 *c*-axes were measured. As shown in Fig. D2(a), they are very inhomogenously distributed, and reflect the presence of two separate groups of crystals with different LPO's so that the mean *c*-axis orientation lies away from the centre of the major cluster (also reflected in the satellite peak in Fig. D1 a). This inhomogeneity is reflected in the histogram. Here, the magnetically determined $K = 13$ (solid curve), corresponding to a presumed rotationally-symmetric distribution, represents a reasonable compromise, and the $K = 29$ (dashed curve) based on results from Fig. D1 and Table E3 suggests a tighter distribution. For sample 36b (Fig. D2 b), only 40 more evenly distributed *c*-axes were determined. The histogram of deviation from the average axis corresponds reasonably to the magnetically estimated value of $K = 9.78$, whereas the value of $K = 26.35$ suggests a tighter distribution. We are still unsure as to

why the distributions (dashed lines) for higher K, determined using EBSD data, are tighter than the distributions (solid lines) for lower K, determined using magnetic data. The magnetic data represent the entire sample, whereas EBSD data represent only measured crystals on two circular sample surfaces. However, this cannot explain the discrepancy between two different ways of presenting the EBSD results.

APPENDIX E: EVALUATING RELATIONSHIPS BETWEEN MEASURED AND CALCULATED PROPERTIES OF NATURAL CRYSTAL ASSEMBLAGES

Using equations in Appendix C, relating NRM and the AMS of generic assemblages of hemo-ilmenite platelets, properties of given assemblages of platelets were calculated, based on selected samples, where the properties change as a result of a different angle α of the statistical (0001) basal plane to the magnetizing field v. These properties were β, the angle the NRM makes with the magnetizing field **v** (Fig. 17); the NRM intensity in A m^{-1} (Fig. 18); and ψ, the angular deviation of the NRM from the statistical (0001) basal plane (Fig. 19).

Calculated curves were based on the function y that derives from ψ and α according to eq. (C10) in Appendix C. Values of ψ and α and calculations of y are given in Appendix D, Table E2 for all samples in groups A and B and three others illustrated in the equal area diagrams of Fig. 13.

Values of y and curves in Figs 17–19 are independent of the AMS except to the extent AMS was used to locate the statistical (0001) basal plane. The Fisher parameter K, as illustrated in Appendix C, Fig. C1, can be calculated for individual values of y as illustrated

Table E1. Measured and calculated AMS data for samples 36b and Le7b.

	Cryst. #19 36b	Hargraves 36b	Calc. Fig. D1(e) 36b	Hargraves Le7b	Calc. Fig. D1(d) Le7b
k_1	6.842[1]	0.037[2]	6.730	0.035[2]	6.723
k_2	6.682	0.035	6.589	0.035	6.634
k_3	4.595	0.030	4.738	0.024	4.710
k_1/k_3	1.489	1.23	1.420	1.46	1.429
k_2/k_3	1.452	1.17	1.391	1.46	1.408
k_1/k_2	1.024	1.06	1.021	1.00	1.013
k_3/k_1	0.672	0.811	0.704	0.686	0.701
k_2/k_2	0.688	0.857	0.719	0.688	0.710
Ave.k_1, k_2	6.762	0.036	6.660	0.035	6.679
k_3/Ave.	0.680	0.833	0.711	0.688	0.705

[1]Recent measurements, volume normalized.
[2]Data are direct from Hargraves (1959a), in emu/cc. Correction to SI not used here. However, rough estimates were obtained from the mean of these numbers, and the results indicate that no magnetite is present in these samples. The ratios are reliable.

Table E2. Calculation of individual y from ψ and α, and k_3/k_1, k_3^0/k_1^0, k_1^0/k_3^0 and k_1/k_3 from AMS data.

Sample	Class	k_1/k_2	ψ	α	y from eq. (C10)	K from y Eq. (C8)	k_3	k_1	k_3/k_1	k_3^0/k_1^0 Eq. (C15)	k	k_1^0/k_3^0	k_1/k_3	
23a	A	1.06	24.2	53.0	0.145	5.69	0.060	0.089	0.674	0.468	0.078	2.136	1.483	
26b	A	1.00	23.1	2.1			0.046	0.084	0.548		0.071		1.826	**D**
33a	A	1.00	1.3	32.0	0.018	55.05	0.102	0.196	0.520	0.498	0.165	2.009	1.922	
33b	A	1.00	50.8	72.5	0.162	4.92	0.100	0.153	0.654	0.392	0.135	2.548	1.53	
35an	A	1.00	33.1	66.0	0.127	6.72	0.025	0.043	0.581	0.378	0.037	2.646	1.720	
35bn	A	1.08	35.2	53.5	0.207	3.42	0.024	0.040	0.600	0.134	0.034	7.465	1.667	**E**
36a	A	1.17	47.0	83.3	0.059	15.81	0.023	0.035	0.657	0.593	0.029	1.686	1.522	
36b	A	1.06	35.0	73.9	0.092	9.78	0.030	0.037	0.811	0.745	0.034	1.342	1.233	
86a	A	1.01	8.1	24.9	0.133	6.34	0.069	0.145	0.476	0.219	0.119	4.571	2.101	
86b	A	1.02	10.0	20.3	0.192	3.85	0.039	0.100	0.390	(-0.130)	0.079		2.564	**F**
206b	A	1.03	7.3	23.0	0.131	6.44	0.063	0.205	0.307	0.007	0.156	145.28	3.254	**E**
216a	A	1.04	41.3	63.2	0.182	4.20	0.065	0.098	0.663	0.348	0.086	2.875	1.508	
216b	A	1.03	20.1	32.9	0.220	3.08	0.078	0.097	0.804	0.487	0.090	2.054	1.244	
216c	A	1.03	23.2	37.7	0.217	3.17	0.083	0.118	0.703	0.282	0.105	3.545	1.422	
Le7a	A	1.00	2.5	53.1	0.016	60.99	0.020	0.030	0.667	0.652	0.027	1.534	1.500	
Le7b	A	1.00	13.9	58.3	0.071	13.00	0.024	0.035	0.686	0.612	0.031	1.635	1.458	
Le64a	A	1.02	18.0	83.3	0.019	52.39	0.044	0.061	0.721	0.706	0.055	1.416	1.386	
Le64b	A	1.03	8.3	74.0	0.020	47.79	0.044	0.064	0.688	0.669	0.057	1.494	1.455	
Gr117a	A	1.03	22.8	53.3	0.135	6.19	0.062	0.122	0.508	0.255	0.101	3.919	1.968	
Gr117b	A	1.08	5.2	36.9	0.057	16.44	0.043	0.119	0.361	0.262	0.091	3.821	2.767	
Nwa219a	A	1.07	38.0	83.3	0.044	21.74	0.060	0.102	0.588	0.535	0.086	1.867	1.700	
Nwa219b	A	1.10	38.0	83.3	0.044	21.74	0.076	0.112	0.679	0.636	0.097	1.573	1.474	
Nwa221a	A	1.01	6.1	35.1	0.071	13.07	0.035	0.147	0.238	0.095	0.109	10.529	4.200	**E**
Nwa221b	A	1.04	3.5	37.2	0.039	24.78	0.037	0.152	0.243	0.171	0.112	5.833	4.108	

Table E2. (*Continued.*)

Sample	Class	k_1/k_2	ψ	α	y from eq. (C10)	K from y Eq. (C8)	k_3	k_1	k_3/k_1	k_3^0/k_1^0 Eq. (C15)	k	k_1^0/k_3^0	k_1/k_3	
La150a	A	1.04	8.6	64.5	0.035	27.69	0.081	0.185	0.438	0.386	0.148	2.593	2.284	
La150b	A	1.09	23.2	73.0	0.061	15.19	0.095	0.187	0.508	0.418	0.151	2.391	1.968	
La152a	A	1.07	8.6	47.2	0.065	14.21	0.112	0.178	0.629	0.552	0.152	1.811	1.589	
La152b	A	1.03	26.2	57.2	0.137	6.11	0.065	0.094	0.691	0.512	0.083	1.955	1.446	
20c	B	1.05	9.8	22.7	0.171	4.56	0.440	0.610	0.721	0.478	0.543	2.090	1.386	
21c	B	1.38	2.3	63.8	0.010	101.19	0.220	0.540	0.407	0.393	0.383	2.544	2.455	
21d	B	1.10	0.3	58.9	0.002	633.20	0.140	0.330	0.424	0.422	0.257	2.369	2.357	
46b	B	1.13	11.0	31.0	0.139	5.98	0.400	0.540	0.741	0.581	0.473	1.722	1.350	
85a	B	1.03	5.2	34.5	0.062	15.03	0.110	0.350	0.314	0.199	0.267	5.020	3.182	
85b	B	1.02	− 6.0	28.5			0.170	0.440	0.386		0.119		2.588	**G**
96b	B	1.06	− 2.8	42.4			0.230	0.550	0.418		0.433		2.391	**G**
105a	B	1.00	7.0	73.2	0.018	53.93	0.205	0.560	0.366	0.338	0.442	2.963	2.732	
112b	B	1.09	6.0	83.3	0.006	161.98	0.208	0.740	0.281	0.271	0.543	3.692	3.558	
212b	B	1.19	23.7	54.9	0.134	6.29	0.150	0.310	0.484	0.227	0.240	4.397	2.067	
213b	B	1.01	32.8	79.0	0.059	15.90	0.198	0.375	0.528	0.445	0.314	2.245	1.894	
214a	B	1.04	0.9	5.0	0.082	11.04	0.210	0.560	0.375	0.223	0.437	4.485	2.667	
214b	B	1.06	12.2	5.5			0.175	0.360	0.486		0.292		2.057	**D**
Gr118a	B	1.16	80.9	83.3	0.268	2.01	0.222	0.412	0.539	(− 0.447)	0.330		1.856	**F**
La147b	B	1.04	2.1	63.0	0.009	107.04	0.178	0.328	0.543	0.532	0.273	1.881	1.843	
46a		1.15	32.6	46.8	0.231	2.83	0.360	0.450	0.800	0.434	0.400	2.304	1.250	
90a		1.13	17.6	64.0	0.072	12.84	0.760	1.360	0.559	0.460	1.107	2.176	1.789	
97b		1.08	19.0	83.3	0.020	49.42	0.680	1.500	0.453	0.425	1.190	2.351	2.206	

Comments:
D: $\alpha < \psi$. **E**: k_1^0/k_3^0 high. **F**: σ^0 negative. **G**: ψ negative.

Table E3. Calculations for 36b and Le7b of y and K from ψ and α, and from k_3/k_1, k_3^0/k_1^0 obtained from AMS and EBSD data.

Sample	ψ	α	y Eq. (C10)	K From y Eq. (C8)	Meas. $k3$	Meas. $k1$	Meas. σ k_3/k_1	Eqn. σ^0 k_3^0/k_1^0 Eq. (C15)	Comment
36b P	35.0	73.9	0.092	**9.78**	0.030	0.037	0.811	0.745	Table E1 and E2
36b R			0.037	**26.35**	4.738	6.730	0.704	0.672	Table E1 AMS Cryst #19. and Fig. D1 (e) (Table E1)
Le7b P	13.9	58.3	0.071	**13.00**	0.024	0.035	0.686	0.612	Table E1 and E2
Le7b R			0.033	**29.55**	4.710	6.723	0.701	0.672	Table E1 AMS Cryst #19. and Fig. D1 (d) (Table E1)

Notes:
Example P: y calculated from ψ and α using eq. (C10). AMS not directly involved. k_3^0/k_1^0 from eq. (C15) and AMS k_3/k_1. Numerical calculation of K from y is from (C8) as illustrated in Fig. C2.
Examples R: y calculated from eq. (C14) or (C15) where k_3^0/k_1^0 from crystal #19 and k_3/k_1 from calc. from EBSD, Fig. D1
Values of K in Fig. D2 are in bold.

in Fig. C2. Furthermore, the curves in Figs 17–19 are related to the angular distribution function K as has been illustrated in Appendix C, Fig. C3, and values of K derived from y are listed in Table E2.

k_3/k_1 and k_3^0/k_1^0 can then be used in a derivative equation to calculate y leading to K, but the y value obtained is identical to the previous result, thus not listed in Table E2. For convenience of comparisons, the values of k_3/k_1 and k_3^0/k_1^0 in Table E2 were also inverted to k_1/k_3 and k_1^0/k_3^0 and plotted alongside the value for mean k, a proxy for susceptibility. In this comparison, the value k_1^0/k_3^0 for single crystals is necessarily larger than k_1/k_3. For samples 36b and Le7b (Table E1) and other typical samples with low susceptibility, k_1^0/k_3^0 is in the range of 1.5–3 and k_1/k_3 in the range of 1.4–2. We can only speculate concerning the cause of the extreme k_1^0/k_3^0 single-crystal values of 3.9–5.8, in samples 86a, Gr117a, Nwa221b, 85a and 214b. We note that such samples all contain at least a trace of magnetite, possibly in a shape fabric parallel to hemo-ilmenite (0001) planes as shown in Fig. 4.